

OASL phase condensation induces amyloid-like fibrillation of RIPK3 to promote virus-induced necroptosis

Received: 26 April 2021

Accepted: 1 November 2022

Published online: 5 January 2023

 Check for updates

Shin-Ae Lee^{1,2,5}✉, Lin-Chun Chang^{2,3,5}✉, WooRam Jung^{1,2}, James W. Bowman², Dokyun Kim^{1,2}, Weiqiang Chen^{1,2}, Suan-Sin Foo^{1,2}, Youn Jung Choi^{1,2}, Un Yung Choi^{1,2}, Anna Bowling¹, Ji-Seung Yoo⁴ & Jae U. Jung^{1,2}✉

RIPK3–ZBP1–MLKL-mediated necroptosis is a proinflammatory cell death process that is crucial for antiviral host defence. RIPK3 self-oligomerization and autophosphorylation are prerequisites for executing necroptosis, yet the underlying mechanism of virus-induced RIPK3 activation remains elusive. Interferon-inducible 2′-5′ oligoadenylate synthetase-like (OASL) protein is devoid of enzymatic function but displays potent antiviral activity. Here we describe a role of OASL as a virus-induced necroptosis promoter that scaffolds the RIPK3–ZBP1 non-canonical necrosome via liquid-like phase condensation. This liquid-like platform of OASL recruits RIPK3 and ZBP1 via protein–protein interactions to provide spatial segregation for RIPK3 nucleation. This process facilitates the amyloid-like fibril formation and activation of RIPK3 and thereby MLKL phosphorylation for necroptosis. Mice deficient in *Oasl1* exhibit severely impaired necroptosis and attenuated inflammation after viral infection, resulting in uncontrolled viral dissemination and lethality. Our study demonstrates an interferon-induced innate response whereby OASL scaffolds RIPK3–ZBP1 assembly via its phase-separated liquid droplets to facilitate necroptosis-mediated antiviral immunity.

Necroptosis is a regulated cell death process that contributes to pathogen-mediated host immune defence by inducing inflammation upon cell death. This intricate balance between induction of inflammatory responses and clearance of pathogens via ‘suicidal death’ is a noteworthy contribution to host–pathogen standoff, as it determines the degree of pathogenic invasion and pathogenicity. Necroptosis signalling is mediated through the formation of a multiprotein complex—the so-called necrosome—in which receptor interacting protein serine/threonine kinase 3 (RIPK3) plays a major effector role. In the absence of

caspase-8-mediated apoptosis, tumour necrosis factor (TNF) induces the assembly of the canonical necrosome complex composed of two RIPKs: RIPK1 and the effector RIPK3 (refs. 1–4). More recently, necroptosis has been recognized as an antiviral mechanism after virus infections, such as murine cytomegalovirus (MCMV)^{5,6}, herpes simplex virus-1 (HSV-1)^{7,8}, vaccinia virus (VACV)² and influenza A virus (IAV)⁹, by forming a non-canonical necrosome composed of RIPK3 and an interferon-stimulated gene (ISG), Z-DNA-binding protein 1 (ZBP1)^{10,11}. RIPK3-mediated phosphorylation of its substrate, mixed lineage kinase

¹Department of Cancer Biology, Infection Biology Program, and Global Center for Pathogen Research and Human Health, Lerner Research Institute, Cleveland Clinic, Cleveland, OH, USA. ²Department of Molecular Microbiology and Immunology, Keck School of Medicine, University of Southern California, Los Angeles, CA, USA. ³Immunology Program of the Sloan Kettering Institute, Memorial Sloan Kettering Cancer Center, New York, NY, USA.

⁴Center for Study of Emerging and Re-emerging Viruses, Korea Virus Research Institute, Institute for Basic Science, Daejeon, Republic of Korea.

⁵These authors contributed equally: Shin-Ae Lee, Lin-Chun Chang. ✉e-mail: lees41@ccf.org; ChangL2@mskcc.org; jungj@ccf.org

domain-like pseudokinase (MLKL), triggers executional signals that increase membrane permeabilization for the release of intracellular damage-associated molecular patterns and thereby elicits a robust antiviral immune response^{12–17}.

RIPK3 autophosphorylation is the primary prerequisite for its self-activation to relay downstream signals for inducing necroptotic cell death; however, this fundamental mechanism remains hypothetical. It has been proposed that intermolecular interactions mediated by the RIP homotypic interaction motif (RHIM) result in high-order hetero-amyloid structures, which may serve as a platform for RIPK3 autophosphorylation^{18–21}. Recent findings have also revealed that artificially induced RIPK3 homo-oligomerization is sufficient to induce necroptosis^{22–24}, which suggests that the kinase activity of RIPK3 could be activated by proximity within RIPK3 oligomers. In addition, RIPK3 assembles into discrete functional amyloid-like foci in the cytosol, but it remains unclear how RIPK3 amyloid formation contributes to necroptosis signalling^{18,25,26}.

The indispensable role of ZBP1 in virus-induced necroptosis, along with other growing evidence, suggests that robust activation of necroptosis during virus infection requires synergistic interplay between type I interferon (IFN) and TNF signalling to intensify the activation of RIPK3 (refs. 27,28). During virus infection, rapid activation of type I IFN signalling gives rise to strong expression of ISGs, among which include the oligoadenylate synthetase (OAS) gene family. OAS family proteins belong to the nucleotidyltransferase superfamily and confer protection against viruses through their 2'-5'-phosphodiester-linked oligoadenylates (2-5As) synthetase activity that is triggered after binding to viral double-stranded RNA (dsRNA). Unlike OAS proteins, the protein OAS-like (OASL) lacks enzymatic activity, yet still has regulatory functions in innate immunity, suggesting that OASL has a role in a RNase L-independent antiviral mechanism. Previous studies have shown that OASL has potent target-specific antiviral activity against a panel of RNA and DNA viruses, enhancing antiviral activity in concert with other ISGs^{29,30}. By contrast, other studies^{31,32} have reported that binding of OASL to RIG-I enhances IFN production during RNA virus infection, whereas binding to cGAS suppresses IFN production during DNA virus infection. Although the definitive antiviral role of OASL remains unclear, the subcellular localization of OASL appeared as distinct foci in the cytoplasm and the nucleus, which suggests that OASL has a behaviour-specific function. These contentious findings prompt further investigation of the precise role of OASL during virus infections.

Liquid–liquid phase separation (LLPS) is an emerging paradigm in the formation of membraneless biomolecular condensates that enables spatiotemporal regulation of biochemical signalling^{33–36}. Liquid droplets serve as a molecular platform to nucleate biomolecules, including proteins and nucleic acids, which discretely tune condition-specific reactions within the complex. Although these liquid condensates are initially highly mobile and dynamic owing to the lack of physical

barriers, many proteins, such as FUS, α -synuclein, and STING, undergo phase transition over time to a more rigid hydrogel or amyloid-like fibril structure^{35–39}. Thus, phase separation facilitates efficient formation of signalling complexes by inducing concentrated homotypic and heterotypic interactions within the partitioned core.

In this study, we identify OASL as a regulator of virus-induced necroptosis that promotes antiviral activity to restrict viral replication and dissemination. OASL undergoes LLPS and chaperones the assembly of RIPK3–ZBP1 necrosome by recruiting RIPK3 and ZBP1 into its phase-separated droplets via protein–protein interactions. These phase condensates serve as a platform for RIPK3 to nucleate, ultimately inducing RIPK3 amyloid-like fibre formation and enzymatic activation. Subsequent activation of the non-canonical necroptosis pathway elicits antiviral activity by restricting virus replication and dissemination *in vivo*. Herein, we elucidate the molecular action of the IFN-inducible OASL as a key signalling adaptor for the RIPK3–ZBP1 necroptotic pathway after virus invasion.

Results

Identification of OASL as a binding partner of RIPK3

MCMV-encoded M45 is a viral inhibitor of RIP activation that blocks necroptosis through the disassembly of the RIPK3–ZBP1 non-canonical necrosome. Thus, we utilized a necroptosis-sensitive mutant MCMV carrying the RHIM mutation of M45 (MCMV-M45mutRHIM) to identify key regulators of the necrosome complex in the context of virus infection^{5,6}. We infected mouse primary tail fibroblasts with the necroptosis-sensitive MCMV-M45mutRHIM, and at 6 h post-infection (h.p.i.), endogenous mouse RIPK3 was immune-purified and subjected to mass spectrometry analysis. In agreement with previous reports¹⁴, a number of TNF signalling proteins and phosphoinositide-related enzymes were specifically detected in the RIPK3 complex after virus infection (Fig. 1a and Supplementary Table 1). Notably, an IFN-inducible protein, OASL1, was detected from the RIPK3 complex following MCMV-M45mutRHIM infection. Mouse OASL1 shares high sequence similarity (74%) with human OASL and is predicted to contain an amino-terminal enzymatically inactive OAS domain (N-OAS) and two carboxy-terminal ubiquitin-like (UBL) domains (C-UBL) like human OASL. By contrast, mouse OASL2 preserves the 2-5As synthesis activity within its N-terminal OAS domain and carries a C-terminal single UBL domain. Co-immunoprecipitation assays showed that RIPK3 specifically interacted with OASL1 but not with OASL2 (Fig. 1b).

OASL is required for efficient virus-induced necroptosis

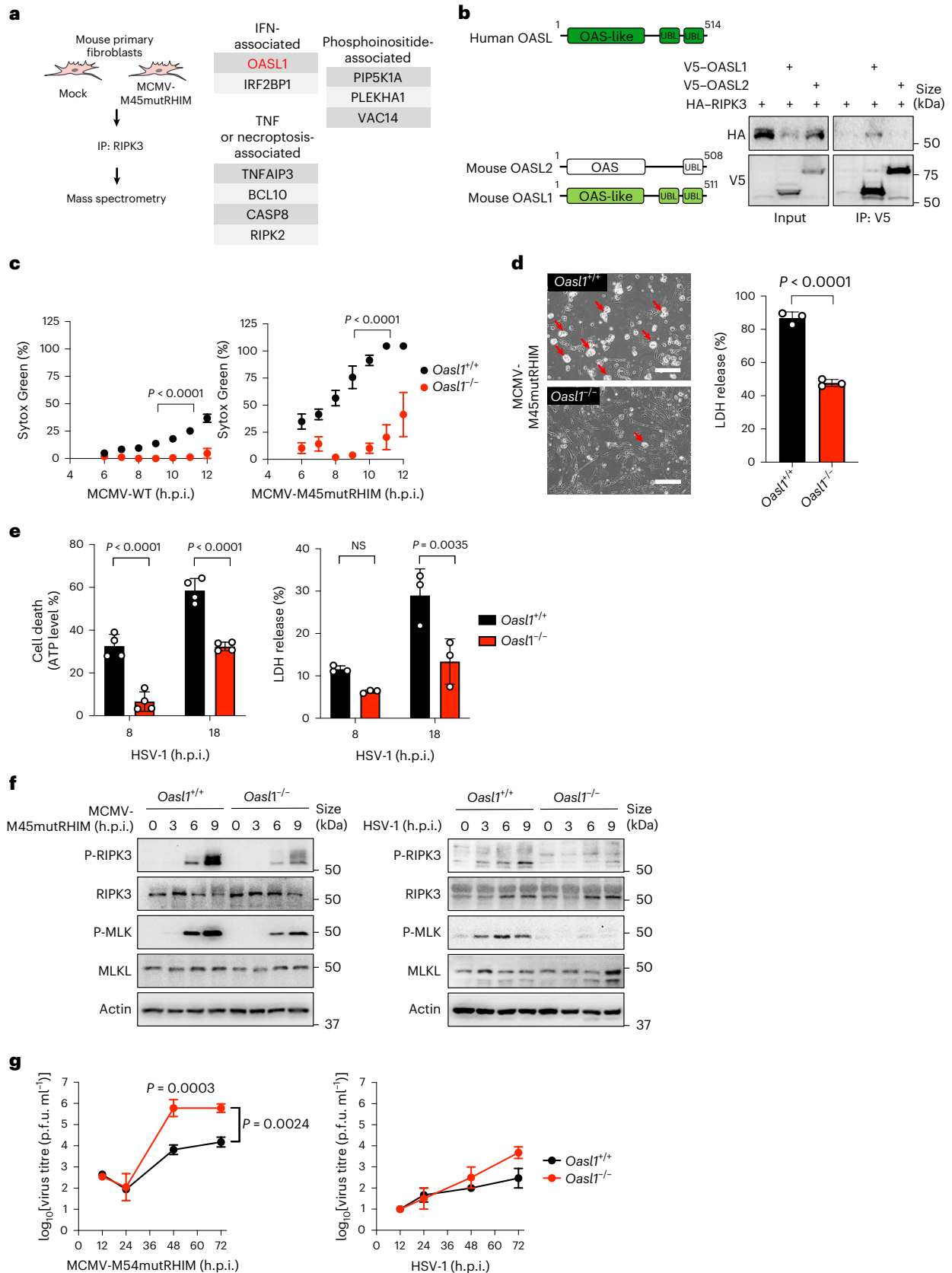
To delineate the mechanism of RIPK3–OASL interactions, we used the CRISPR–Cas9 system to generate an OASL1 homozygous null knockout (*Oasl1*^{-/-}) mouse model (Extended Data Fig. 1a,b). *Oasl1* knockout was confirmed by sequencing and checking the protein expression level in primary tail fibroblasts isolated from wild-type (*Oasl1*^{+/+}) mice and

Fig. 1 | The IFN-stimulated protein OASL is required for efficient virus-induced necroptosis. **a**, Mouse primary fibroblasts were mock-infected or infected with MCMV-M45mutRHIM virus (multiplicity of infection (m.o.i.) = 5) for 6 h. RIPK3 protein complexes were enriched and immunoprecipitated (IP) using RIPK3 antibody-conjugated agarose beads and analysed by mass spectrometry. Functional-related or biological-related proteins are grouped in boxes. **b**, HEK 293T cells were transfected with the indicated constructs, and cell lysates were immunoprecipitated with V5-specific antibody. Immunoprecipitates and whole cell extracts (input) were analysed by immunoblotting with the indicated antibodies. **c**, Cell death kinetics of *Oasl1*^{+/+} and *Oasl1*^{-/-} primary fibroblasts infected with MCMV-WT or MCMV-M45mutRHIM (m.o.i. = 5). Necrotic cell death was measured on the basis of the uptake of Sytox Green and quantified in real-time from 4 to 12 h.p.i. ($n = 4$ biological replicates). **d**, Left: microscopy analysis of cell death in *Oasl1*^{+/+} and *Oasl1*^{-/-} primary fibroblasts infected with MCMV-M45mutRHIM at 16 h.p.i. Arrows indicate cells with necrotic features after infection. Scale bar, 20 μ m. Right: quantification of necrotic cell death

by measuring the release of LDH from *Oasl1*^{+/+} and *Oasl1*^{-/-} primary fibroblasts infected with MCMV-M45mutRHIM (m.o.i. = 5) for 8 h. **e**, Quantification of necrotic cell death by measuring intracellular ATP levels ($n = 4$) and LDH release ($n = 3$) in supernatants of *Oasl1*^{+/+} and *Oasl1*^{-/-} primary fibroblasts infected with HSV-1 (m.o.i. = 5). **f**, Immunoblot analysis of RIPK3 and MLKL phosphorylation (P-RIPK3 and P-MLKL, respectively) in *Oasl1*^{+/+} and *Oasl1*^{-/-} primary fibroblasts infected with MCMV-M45mutRHIM (left) or HSV-1 (right) at m.o.i. = 5 for the indicated hours. Infected cells were collected and subjected to immunoblotting with the indicated antibodies. **g**, Viral replication of MCMV-M45mutRHIM and HSV-1 in *Oasl1*^{+/+} ($n = 4$ for MCMV-M45mutRHIM, $n = 3$ for HSV-1) and *Oasl1*^{-/-} ($n = 2$) primary fibroblasts were determined by plaque assays by titrating culture supernatants at the indicating time points. Data are representative of two (**b,f,g**) or three (**c–e**) independent experiments. For **c–e,g**, data are presented as the mean \pm s.e.m. Statistical analyses were performed using two-tailed unpaired *t*-test (**d**) or two-way analysis of variance (ANOVA) (**c–e,g**). NS, not significant.

Oasl1^{-/-} mice (Extended Data Fig. 1c,d). OASL did not exhibit a crucial role in TNF-mediated canonical necroptosis (Extended Data Fig. 1e), whereas *Oasl1*^{+/+} and *Oasl1*^{-/-} primary mouse fibroblasts exhibited pronounced differences in virus-induced necroptosis upon infection

with wild-type MCMV (MCMV-WT) or MCMV-M45mutRHIM during a real-time cytotoxicity assay (Fig. 1c). *Oasl1*^{+/+} fibroblasts showed low levels of cell death upon MCMV-WT infection but near complete death by 11 h.p.i. upon MCMV-M45mutRHIM infection (Fig. 1c).



Conversely, both the magnitude and kinetics of cell death were considerably reduced in *Oasl1*^{-/-} fibroblasts upon MCMV-M45mutRHIM infection (Fig. 1c, right). MCMV-M45mutRHIM-induced necrotic cell death, featured by cytoplasmic swelling (Fig. 1d, left), was extensive in *Oasl1*^{+/+} fibroblasts starting from 6 h.p.i. and continuously increased until 11 h.p.i., whereas it was weak in *Oasl1*^{-/-} fibroblasts (Fig. 1c, right). The level of lactate dehydrogenase (LDH) release upon MCMV-M45mutRHIM infection was significantly lower in *Oasl1*^{-/-} fibroblasts than in *Oasl1*^{+/+} fibroblasts, but minimal in both cells upon MCMV-WT infection (Fig. 1d, right, and Extended Data Fig. 1f). In addition, HSV-1 infection, which has previously been reported to promote ZBP1–RIPK3-dependent necroptosis^{7,8}, led to significantly reduced cell death in *Oasl1*^{-/-} fibroblasts compared with *Oasl1*^{+/+} fibroblasts as measured by the levels of LDH release and intracellular ATP (Fig. 1e). These results indicate that OASL1 plays a crucial role in mediating virus-induced necroptotic cell death.

The hallmarks of necroptosis activation are RIPK3 autophosphorylation (human RIPK3 at Ser227; mouse RIPK3 at Thr231 and Ser232)^{23,40} and MLKL phosphorylation (human MLKL at Thr357 and Ser385; mouse MLKL at Ser345)²⁵. Corresponding to the magnitudes of cell death observed in *Oasl1*^{+/+} and *Oasl1*^{-/-} fibroblasts (Fig. 1c), MCMV-M45mutRHIM infection-induced RIPK3 phosphorylation was drastically reduced in *Oasl1*^{-/-} fibroblasts compared with *Oasl1*^{+/+} fibroblasts (Fig. 1f, left). Consistently, *Oasl1*^{-/-} fibroblasts showed markedly reduced MLKL phosphorylation compared with *Oasl1*^{+/+} fibroblasts (Fig. 1f, left). These correlative patterns of cell death and necroptosis activation were readily observed following necroptosis-sensitive HSV-1 infection, but not after necroptosis-resistant MCMV-WT infection (Fig. 1f, right, and Extended Data Fig. 1g). Consequently, *Oasl1*^{-/-} fibroblasts that showed substantially lower levels of necroptosis displayed higher MCMV-M45mutRHIM or HSV-1 titres than *Oasl1*^{+/+} fibroblasts (Fig. 1g). By contrast, MCMV-WT replicated at comparable levels in both *Oasl1*^{+/+} and *Oasl1*^{-/-} fibroblasts (Extended Data Fig. 1h). Additionally, CRISPR–Cas9-mediated ablation of *Oasl1* in necroptosis-sensitive A549 human lung epithelial cells exhibited a significant reduction in cell death upon HSV tagged with green fluorescent protein (HSV–GFP) or VACV infection (Extended Data Fig. 1i). These data collectively indicate that OASL1 promotes RIPK3–MLKL-mediated necroptosis during virus infection to restrict viral replication.

OASL chaperones the assembly of the RIPK3–ZBP1 necrosome

The RHIM-mediated interaction between ZBP1 and RIPK3 forms a non-canonical necrosome during virus infection^{6,41,42}. More recently, the Zα domains of ZBP1 were reported to be essential for ZBP1-mediated necroptosis, but the precise role of the Zα domains in RIPK3–ZBP1 interactions during virus infection remains elusive^{43,44}. To test whether OASL might play a role in the assembly of the RIPK3–ZBP1 necrosome, MCMV-M45mutRHIM-infected *Oasl1*^{+/+} and *Oasl1*^{-/-} primary fibroblasts were collected at 8 h.p.i. for immunoprecipitation with an anti-RIPK3

antibody. RIPK3–ZBP1 interaction was readily detected in *Oasl1*^{+/+} fibroblasts, whereas the interaction was barely detected in *Oasl1*^{-/-} fibroblasts (Fig. 2a). In addition, the RIPK3–OASL1 interaction was evidently detected in *Oasl1*^{+/+} fibroblasts (Fig. 2a). Immunoblotting with an anti-PKR antibody was included as a negative control. The RIPK3–ZBP1 interaction was further probed in *Oasl1*^{+/+} and *Oasl1*^{-/-} primary fibroblasts by in situ proximity ligation assay (PLA). *Oasl1*^{+/+} primary fibroblasts displayed numerous PLA puncta as early as 4 h.p.i. and gradually increased to a peak at 6 h.p.i., whereas *Oasl1*^{-/-} primary fibroblasts exhibited minimal numbers of PLA puncta during the course of infection (Fig. 2b,c and Extended Data Fig. 2a,b). These data suggest that OASL is a crucial mediator in the formation of the RIPK3–ZBP1 necrosome during virus-induced necroptosis.

To further characterize the interaction of OASL and RIPK3, we truncated OASL into the N-OAS domain and the C-UBL domain and identified that RIPK3 bound to N-OAS (Fig. 2d). The serine/threonine kinase RIPK3 has an N-terminal kinase domain and a C-terminal proline-rich region adjacent to the single RHIM (Fig. 2e). Co-immunoprecipitation revealed that the C-terminal proline-rich/RHIM-containing domain, but not the N-terminal kinase domain, of RIPK3 interacted with OASL as efficiently as full-length RIPK3 (Fig. 2e). Notably, human OASL also effectively interacted with human ZBP1 in a transient expression assay (Extended Data Fig. 2c). ZBP1 carries two Z-DNA-binding domains (Zα and Zβ) at the N terminus and a pair of adjacent RHIM motifs at the C terminus (Fig. 2f). Owing to the small size of the Zα and Zβ domains, we utilized a yeast two-hybrid system to dissect the protein–protein interaction and revealed that the N-terminal Zα domain of ZBP1 bound to OASL1 as effectively as full-length ZBP1 (Fig. 2f). Furthermore, ZBP1 specifically interacted with OASL1, but not OASL2, and the C-UBL domain of OASL1 was crucial for the interaction with ZBP1 (Extended Data Fig. 2d). To test the functional consequence of these interactions, *Oasl1*^{-/-} primary fibroblasts were complemented with full-length OASL or with the N-OAS or C-UBL domain of OASL1, followed by MCMV-M45mutRHIM or HSV-1 infection to induce necroptosis. Compared with expression of the control vector, expression of full-length OASL1 readily enhanced RIPK3-mediated MLKL Ser345 phosphorylation in *Oasl1*^{-/-} fibroblasts infected with MCMV-M45mutRHIM or HSV-1 (Fig. 2g). Subsequently, full-length OASL1 expression in *Oasl1*^{-/-} primary fibroblasts resulted in significantly higher RIPK3-mediated cell death in HSV-1-infected *Oasl1*^{-/-} fibroblasts (Fig. 2g,h). However, neither N-OAS nor C-UBL expression alone was able to reach the level of MLKL phosphorylation and necrotic cell death as robustly as full-length OASL1 expression. This result highlights the requirement of full-length OASL to induce maximal level of necroptosis upon virus infection. Overall, these data indicate that the interactions of OASL with RIPK3 and ZBP1 through its N-OAS and C-UBL domains, respectively, are crucial for RIPK3–ZBP1 assembly and virus-induced necroptosis, thereby establishing OASL as a chaperone for the formation of the non-canonical necrosome (Extended Data Fig. 2e).

Fig. 2 | OASL chaperones the assembly of the RIPK3–ZBP1 necrosome complex.

a, *Oasl1*^{+/+} and *Oasl1*^{-/-} primary fibroblasts were infected with MCMV-M45mutRHIM (m.o.i. = 5) for 0 or 8 h. Whole-cell lysates were immunoprecipitated using an anti-RIPK3 antibody, followed by immunoblot analysis using the indicated anti-ZBP1, anti-OASL1, anti-RIPK3 or anti-PKR antibody. **b,c**, In situ PLA using anti-RIPK3 and anti-ZBP1 antibodies in *Oasl1*^{+/+} and *Oasl1*^{-/-} primary fibroblasts infected with MCMV-M45mutRHIM (m.o.i. = 5) for 0 or 6 h. Fluorescence microscopy was used to detect the discrete fluorescent PLA signals (red dots). Representative images of dots indicate the interaction of endogenous RIPK3 and ZBP1. Scale bar, 10 μm. **c**, Quantification of the dot signals of **b** per cell ($n = 32$ cells). Each dot indicates a single cell. **d,e**, HEK 293T cells were transfected with the indicated Flag, HA, V5 or untagged constructs, and cell lysates were immunoprecipitated with anti-RIPK3 (**d**) or anti-HA antibodies (**e**). Immunoprecipitates and whole cell extracts (input) were analysed by

immunoblotting with the indicated antibodies. **f**, AH109 yeasts were transformed with pGBKT7-OASL1 or pACT2-ZBP1 constructs. Interactions were determined by triple dropout (Trp–Leu–His–) synthetic medium or secreted α -galactosidase activity assay using X-Gal. **g**, OASL1-mediated phosphorylation of the necroptosis effector MLKL. *Oasl1*^{-/-} primary fibroblasts were complemented with empty vector (Vector), HA-tagged full-length OASL1, N-OAS domain or C-UBL domain and infected with MCMV-M45mutRHIM or HSV-1 (m.o.i. = 5) for the indicated times. Total cell lysates were subjected to immunoblot analysis with the indicated antibodies. **h**, Measurement of necrotic cell death on the basis of released LDH in *Oasl1*^{-/-} primary fibroblasts reconstituted with empty vector or the indicated OASL1 constructs infected with HSV-1 (m.o.i. = 5) at various time points. Data are representative of two (**b–f**) or three (**a,g,h**) independent experiments. For **c,h**, data are presented as the mean \pm s.e.m. and statistical analysis was performed using two-way ANOVA.

concentration of 0.05 μM (Fig. 3a). The frequency and size of the OASL droplets correlatively increased with the increasing concentrations of OASL (Extended Data Fig. 3d). Notably, N-OAS was sufficient to undergo LLPS as efficiently as full-length OASL, whereas C-UBL did not form any liquid droplets (Fig. 3a and Extended Data Fig. 3d). The dynamic activity of OASL droplets was demonstrated by the increase in droplet size over time (Fig. 3b), whereby liquid droplets coalesced after coming into contact with one another to form larger droplets (Fig. 3c). Furthermore, a time-course spectrometric assay that measures protein turbidity showed a considerable increase in OASL or N-OAS phase separation, but not for C-UBL (Fig. 3d). In accordance with previous studies^{47,48}, increasing the salt concentration or incubation with the aliphatic chemical 1,6-hexanediol considerably disrupted OASL droplet formation (Extended Data Fig. 3e,f). Conversely, as divalent cations control phase separation^{49,50}, increasing the concentration of Mg^{2+} ions increased the size of OASL droplets (Extended Data Fig. 3g).

Refractive index (RI), a measure of intrinsic optical property, enables the characterization of intracellular structures in a label-free and noninvasive manner^{51,52}. A combination of three-dimensional (3D) holotomographic and fluorescence imaging of purified OASL-GFP liquid droplets defined OASL droplets at specific RI values, which enabled quantitative measurement of the morphological and biochemical properties of OASL droplets (Fig. 3e,f). 3D RI tomograms quantitatively demonstrated the increases in volume and surface area of the OASL droplets, as well as the mass and concentration of OASL within the droplets after phase-separation induction. The results correlated with the increased mean RI values (Fig. 3f), which indicated that the droplets fuse over time. In addition, the average sphericity index of the OASL droplets was 0.8368 ± 0.005769 after phase-separation induction, which indicated that the droplets are a near-perfect spherical shape (Fig. 3f). These results suggest that OASL, but not RIPK3 or ZBP1, forms liquid droplets that are fused over time and increase in size and mass.

N-OAS that sufficiently undergoes phase separation contains a dsRNA-binding groove⁵³. Notably, OASL droplet formation increased in frequency following treatment with poly(I:C) low molecular weight (LMW), and a large increase in frequency and size was observed after longer treatment with poly(I:C) high molecular weight (HMW) in vitro (Fig. 3g). As seen with OASL-GFP, fluorescence-labelled untagged human OASL, as well as mouse OASL1-GFP, formed phase-separated droplets that were further enhanced after poly(I:C) HMW treatment (Extended Data Fig. 3h–i). Accordingly, RNase A treatment disrupted in vitro OASL phase separation (Fig. 3g). Furthermore, a dsRNA-binding-deficient OASL mutant (OASL-RK; R45E, K66E, R196E and K201E) failed to undergo LLPS in vitro (Fig. 3h). These results indicate that binding of dsRNA contributes to the in vitro phase separation of OASL.

OASL phase condensates after virus infection

To assess the biological role of OASL phase separation in the context of virus infection, *Oas1l*^{-/-} primary fibroblasts expressing WT

OASL1-mCherry or the dsRNA-binding mutant OASL1-RK-mCherry were infected with MCMV-M45mutRHIM. WT OASL1-mCherry was observed as discrete cytosolic foci after MCMV-M45mutRHIM infection that specifically colocalized with dsRNA-containing granules stained by the dsRNA-specific antibody J2 (ref. 54) (Fig. 3i). By contrast, the OASL1-RK mutant showed little or no cytoplasmic foci formation upon MCMV-M45mutRHIM infection (Fig. 3j). We next examined the dynamics of OASL1 foci in virus-infected live cells using fluorescence recovery after photobleaching (FRAP) assay. Cytoplasmic foci stained with SYTO Blue, a cell-permeable double-stranded nucleic acid dye, were extensively colocalized with OASL1-mCherry foci in MCMV-M45mutRHIM-infected *Oas1l*^{-/-} primary fibroblasts (Fig. 3k). After partially photobleaching a section of the SYTO-stained OASL1-mCherry foci, the fluorescent signal underwent rapid and near-complete recovery by 120 s after bleaching (Fig. 3k, bottom, and Supplementary Video 1). These OASL droplets featured dynamic liquid-like phase condensation and continuous exchange between the foci and the surrounding environment during virus-induced necroptosis (Supplementary Video 1). To further assess whether the OASL droplets display propensity for liquid-to-solid-like transition, FRAP curves were acquired during early and late time points of MCMV-M45mutRHIM infection. Notably, the fluorescence recovery of the droplets was faster and higher at 4 and 6 h.p.i. than at 8 h.p.i. (Fig. 3l, Extended Data Fig. 3j,k and Supplementary Videos 1–3). As liquid droplets exhibit changes in viscoelasticity during droplet maturation³⁷, our data suggest that OASL1 foci may manifest a transition from a liquid-like state to a gel-like state over time during virus infection. Overall, these results demonstrate that OASL dynamically phase condensates into dsRNA-containing liquid droplets during virus-induced necroptosis.

OASL recruits RIPK3 and ZBP1 into its phase condensate to activate RIPK3

Although purified RIPK3 or ZBP1 was unable to undergo phase separation in vitro (Extended Data Fig. 3b,c), incubation with OASL-GFP efficiently recruited RIPK3_{295–518}-mCherry and ZBP1-BFP into OASL droplets in vitro (Fig. 4a). The C-terminal RIPK3_{295–518} that mediated interactions with OASL was sufficient for recruitment into either full-length OASL or N-OAS droplets, but not C-UBL (Extended Data Fig. 4a). mCherry-tagged full-length RIPK3 incubated with purified untagged OASL, N-OAS or C-UBL also showed efficient droplet formation following incubation with OASL or N-OAS, but not C-UBL (Extended Data Fig. 4b). Furthermore, induction of all three proteins together showed that both RIPK3_{295–518}-mCherry and ZBP1-BFP were sequestered into OASL-GFP droplets, forming a triple protein condensate in vitro (Fig. 4b). To assess whether RIPK3 and ZBP1 condensed together into OASL liquid droplets during virus infection, *Oas1l*^{-/-} primary fibroblasts complemented with OASL1-mCherry were infected with MCMV-M45mutRHIM and subsequently immune-stained

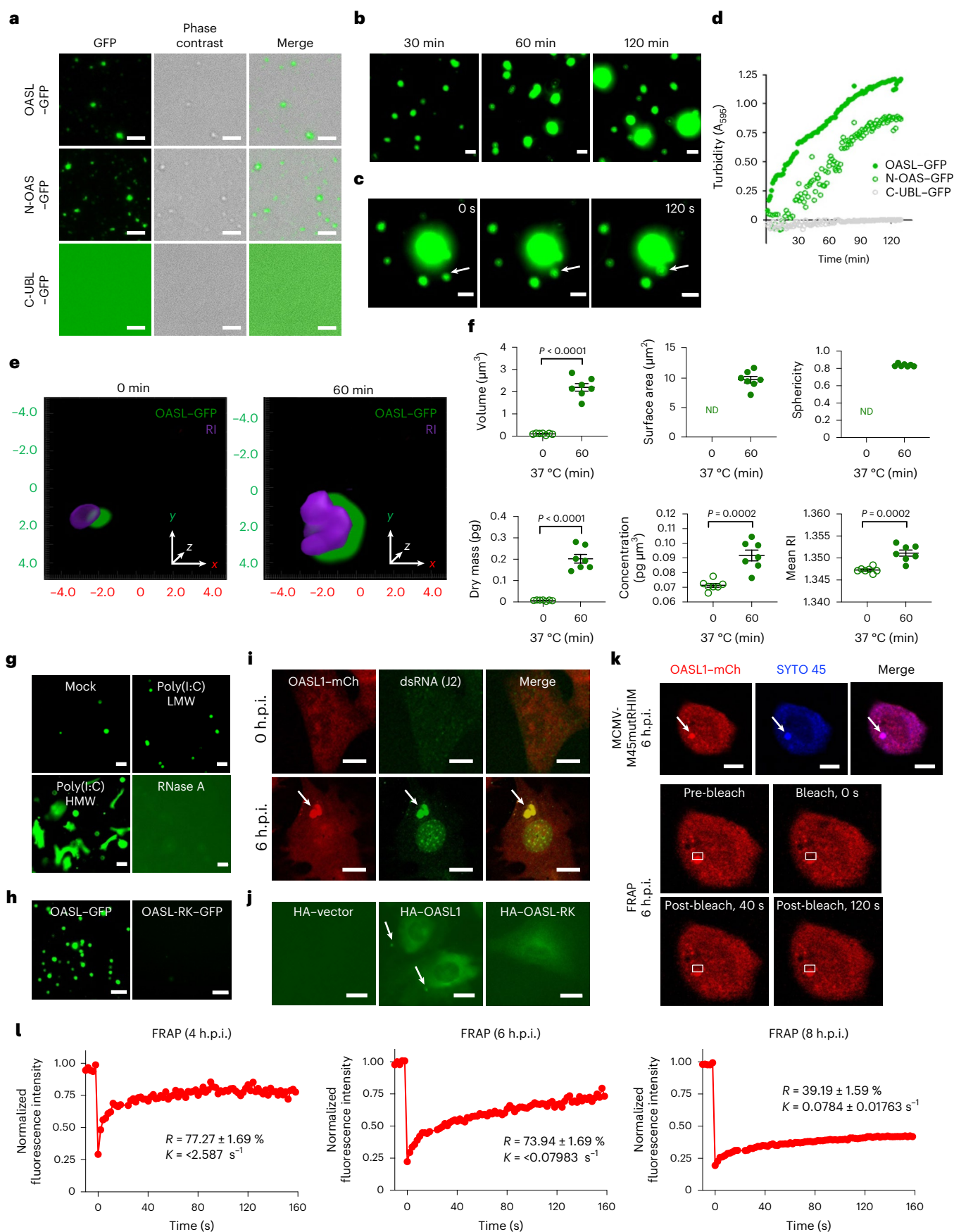
Fig. 3 OASL undergoes LLPS during virus-induced necroptosis.

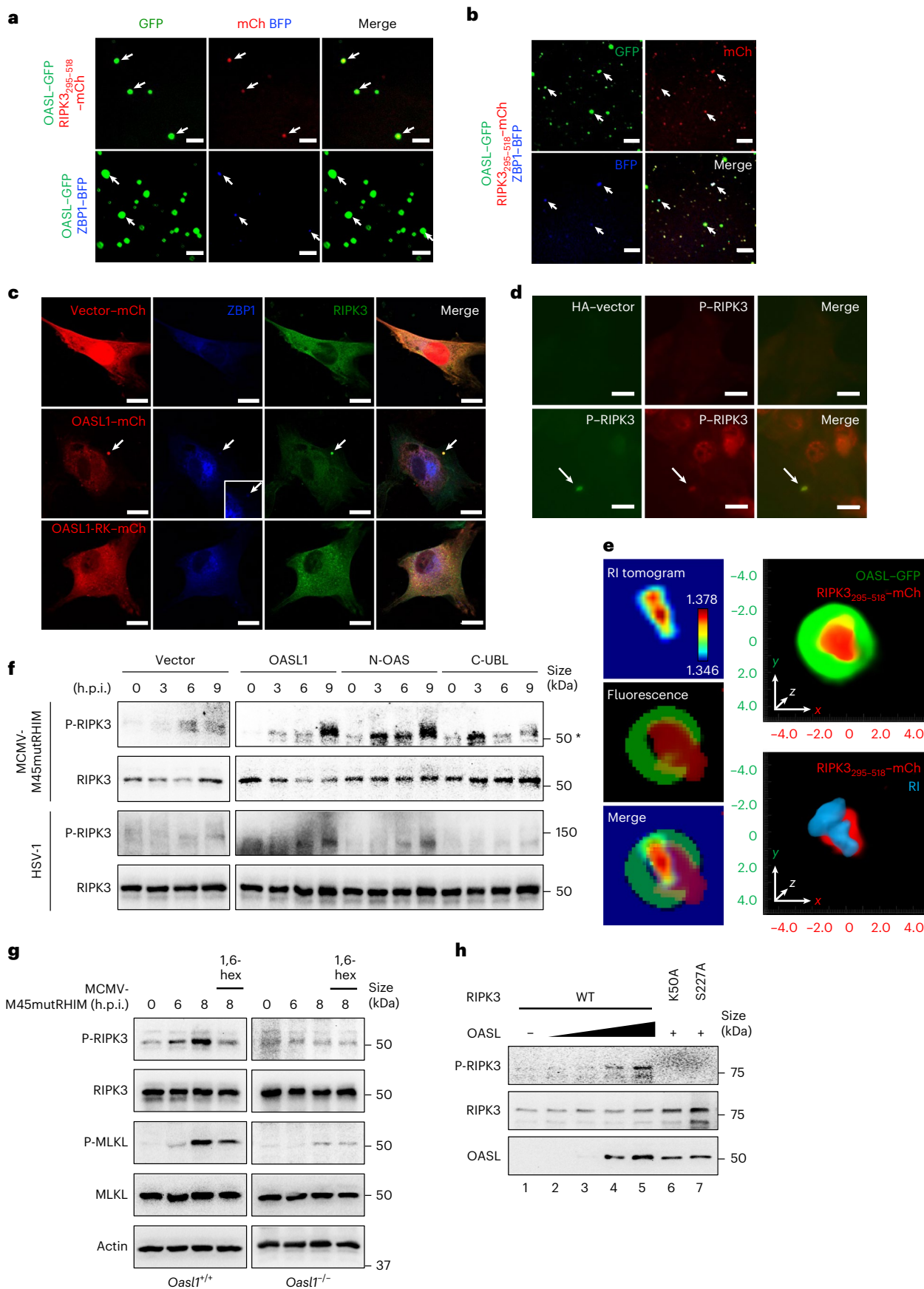
a, Fluorescence images of droplet formation by GFP-tagged full-length OASL, and the N-OAS and C-UBL domains of OASL in vitro 30 min after induction. **b**, LLPS of GFP-tagged OASL over time in vitro. **c**, Time-lapse images of the coalescence of OASL liquid droplets over 120 s (indicated by the arrow). **d**, Turbidity measurement of GFP-tagged full-length OASL, and the N-OAS and C-UBL domains of OASL over time in vitro. **e**, Representative 3D RI distribution and fluorescence of OASL droplets before and after incubation at physiological conditions (green, GFP fluorescence; purple, RI tomogram; $n = 50$ condensates per condition). **f**, Statistical analyses of morphological (top) and biochemical (bottom) parameters of **e** ($n = 7$ condensates per condition). ND, not detected. **g**, Representative images of OASL-GFP (0.05 μM) phase separation mixed with poly(I:C) LMW (50 $\mu\text{g ml}^{-1}$), poly(I:C) HMW (50 $\mu\text{g ml}^{-1}$) or RNase A (300 $\mu\text{g ml}^{-1}$) for 60 min. **h**, Droplet formation of full-length OASL-GFP and the dsRNA-binding mutant OASL-RK-GFP. **i**, Representative images of *Oas1l*^{-/-} primary fibroblasts reconstituted with OASL1-mCherry (OASL1-mCh) and infected

with MCMV-M45mutRHIM. Viral dsRNA was immunostained with J2 antibody. **j**, Representative images of *Oas1l*^{-/-} primary fibroblasts reconstituted with HA-vector, HA-OASL1 or HA-OASL1-RK and infected with MCMV-M45mutRHIM. Arrows indicate discrete OASL1 foci in the cytosol. **k**, Top: arrows indicate the SYTO-45-stained OASL1-mCherry area chosen for photobleaching. Bottom: representative images of OASL1-mCherry foci before and after photobleaching ($n = 3$ cells). Rectangle frames represent the bleached and recovered area within the targeted area. **l**, Quantitative FRAP of OASL1 and SYTO 45 foci for 160 s in *Oas1l*^{-/-} fibroblasts reconstituted with OASL1-mCherry and infected with MCMV-M45mutRHIM for 4, 6 or 8 h. Calculated exponential constant (K) and normalized plateau after fluorescence recovery (R) are the mean \pm s.e.m. ($n = 2$ OASL1 and SYTO 45 foci). Images are representative of five (**a–c,g,h**), three (**d–f,i,j**) or two (**k,l**) independent experiments. For **f**, data are presented as the mean \pm s.e.m. and statistical analysis was performed using two-tailed unpaired t -test. Scale bars, 10 μm (**a–c,g,i–k**) or 30 μm (**h**).

for endogenous RIPK3 and ZBP1. Expression of OASL1-mCherry effectively sequestered both RIPK3 and ZBP1 into its condensate in the cytoplasm during virus infection (Fig. 4c and Extended Data

Fig. 4c,d). By contrast, RIPK3 and ZBP1 were diffusely localized in MCMV-M45mutRHIM-infected *Oasl1*^{-/-} fibroblasts expressing vector or OASL1-RK-mCherry (Fig. 4c).





Oasl1^{-/-} primary fibroblasts reconstituted with haemagglutinin-tagged OASL1 (HA-OASL1) formed discrete cytosolic condensates after MCMV-M45mutRHIM infection that precisely colocalized with

phospho-RIPK3-positive foci. By contrast, no specific staining was observed in vector-expressing cells (Fig. 4d). 3D holotomography fluorescence imaging of purified OASL-GFP and RIPK3₂₉₅₋₅₁₈-mCherry

Fig. 4 | OASL liquid droplets recruit RIPK3 and ZBP1 to activate RIPK3.

a, Phase separation of OASL-GFP (0.05 μ M) incubated with RIPK3₂₉₅₋₅₁₈-mCherry (top; 2 μ M) or ZBP1-BFP (bottom; 1 μ M). **b**, Representative images of OASL-GFP, RIPK3₂₉₅₋₅₁₈-mCherry and ZBP1-BFP phase separation 1 h after induction. **a, b**, Arrows indicate colocalized droplets. **c**, *Oas1l*^{-/-} fibroblasts reconstituted with mCherry-tagged vector, OASL1 or OASL1-RK, infected with MCMV-M45mutRHIM and immunostained for endogenous ZBP1 and RIPK3. Arrows indicate complex stained positive for OASL1, ZBP1 and RIPK3. Inset represents a zoomed view of cytosolic ZBP1 foci. **d**, MCMV-M45mutRHIM-infected *Oas1l*^{-/-} primary fibroblasts reconstituted with empty vector or HA-tagged full-length OASL1. Arrow indicates OASL1 and P-RIPK3 foci in the cytosol. **e**, Left: 2D RI tomogram of RIPK3₂₉₅₋₅₁₈-mCherry and fluorescence image of OASL-GFP and RIPK3₂₉₅₋₅₁₈-mCherry. Right, top: 3D fluorescence image of OASL-GFP and RIPK3₂₉₅₋₅₁₈-mCherry. Right, bottom: 3D fluorescence and

RI tomogram of RIPK3₂₉₅₋₅₁₈-mCherry. **f**, Immunoblot of *Oas1l*^{-/-} primary fibroblasts complemented with HA-tagged vector, OASL1, N-OAS or C-UBL and infected with MCMV-M45mutRHIM or HSV-1 (m.o.i. = 5) for the indicated times (asterisk indicates a nonspecific band). **g**, Immunoblot of RIPK3 and MLKL phosphorylation in *Oas1l*^{+/+} and *Oas1l*^{-/-} primary fibroblasts infected with MCMV-M45mutRHIM (m.o.i. = 5) for the indicated hours and pretreated with or without 1% 1,6-hexanediol (1,6-hex) for 2 h. **h**, In vitro kinase reactions were conducted by incubating with purified human WT RIPK3 or a kinase-dead mutant (K50A) or a phosphorylation-deficient mutant (S227A) of human RIPK3 with increasing amounts of purified human OASL protein. Reactions were subjected to SDS-PAGE, and the Ser227 autophosphorylation and input levels of RIPK3 and OASL were evaluated. Data are representative of five (**a, b, e**) or three (**c, d, f, g, h**) independent experiments, with similar results obtained. Scale bars, 10 μ m (**a-d**).

also revealed that RIPK3 was highly concentrated within OASL droplets (Fig. 4e). RI tomograms displayed an increase in RI values towards the core of the OASL droplet, ranging from 1.346 to 1.378, which typically define protein condensates⁵⁵ (Fig. 4e, left). Moreover, the volume, concentration and mean RI of RIPK3₂₉₅₋₅₁₈-mCherry were substantially increased after incubation with OASL-GFP (Extended Data Fig. 4e). To further examine the effect of OASL phase separation on RIPK3 kinase activity, *Oas1l*^{-/-} primary fibroblasts were complemented with OASL1, N-OAS or C-UBL, followed by MCMV-M45mutRHIM or HSV-1 infection. Expression of OASL1 or N-OAS induced robust RIPK3 autophosphorylation, whereas expression of C-UBL or vector marginally induced autophosphorylation (Fig. 4f). Furthermore, treatment with 1,6-hexanediol, which disrupts OASL droplet formation (Extended Data Fig. 3f), led to a considerable reduction in RIPK3 and MLKL phosphorylation in MCMV-M45mutRHIM-infected *Oas1l*^{+/+} primary fibroblasts (Fig. 4g). In addition, in vitro kinase reaction assays demonstrated that increasing the amount of OASL correlatively increased RIPK3 autophosphorylation level, whereas no effect was observed on the phosphorylation of a RIPK3-K50A kinase-dead mutant or a RIPK3-S227A phosphorylation-dead mutant (Fig. 4h). Both the in vitro phase-separation assays and the virus infection study collectively show that OASL drives the condensation of RIPK3 and ZBP1 by recruiting them into its liquid droplets via protein-protein interactions, which ultimately induces RIPK3 autophosphorylation.

OASL phase condensate promotes RIPK3 amyloid-like fibril formation

Notably, staining with thioflavin T (ThT), an aromatic cross β -sheet-specific dye for amyloid-like structures, detected endogenous RIPK3 foci in MCMV-M45mutRHIM-infected *Oas1l*^{+/+} primary fibroblasts that resembled previously reported RIPK3 amyloid fibrils (Fig. 5a) (ref. 18). By contrast, MCMV-M45mutRHIM-infected *Oas1l*^{-/-} or mock-infected *Oas1l*^{+/+} and *Oas1l*^{-/-} primary fibroblasts showed

diffuse cytoplasmic localization of endogenous RIPK3 without any distinct ThT-positive staining (Fig. 5a and Extended Data Fig. 5a). Furthermore, RIPK3₂₉₅₋₅₁₈-mCherry fibril formation substantially increased after in vitro incubation with OASL in a dose-dependent manner (Extended Data Fig. 5b, c). In particular, KCl was more efficient in inducing OASL-mediated RIPK3₂₉₅₋₅₁₈-mCherry fibril formation than NaCl (Extended Data Fig. 5c). Finally, ThT-positive RIPK3₂₉₅₋₅₁₈-mCherry fibrils were readily observed after in vitro incubation with OASL or N-OAS, but not with C-UBL (Fig. 5b and Extended Data Fig. 5d). These data collectively indicate that the N-OAS domain of OASL is vital for efficient RIPK3 fibril formation.

Phase-separated structures provide a platform for protein nucleation, which often results in a transition from a highly mobile liquid-state to a gel-like state owing to the increase in viscoelasticity^{37,38,56,57}. High-resolution transmission electron microscopy (TEM) showed that OASL formed dense, fibril-like structures inside the liquid droplets (Fig. 5c). Incubation of OASL with RIPK3₂₉₅₋₅₁₈ induced amyloid-like fibril formation within the OASL liquid droplets (Fig. 5c). These RIPK3₂₉₅₋₅₁₈ amyloid fibrils, detected by anti-RIPK3 immunogold labeling, within the OASL droplets were dense and extensively branched following incubation with ZBP1 (Fig. 5c and Extended Data Fig. 5e). 3D electron tomograms reconstructed from consecutive virtual sections of TEM images with incrementally tilted angles revealed that whereas RIPK3₂₉₅₋₅₁₈ alone formed irregular and short fibril intermediates¹⁸, incubation with ZBP1 or OASL led to elongated amyloid fibril formation (Fig. 5d and Extended Data Fig. 5f, g). In particular, incubation with OASL led to highly ordered and homomorphic amyloid formation, whereas incubation with the RHIM-containing ZBP1 resulted in irregular and polymorphic amyloid structures (Fig. 5d and Extended Data Fig. 5f, g). Finally, RIPK3₂₉₅₋₅₁₈ amyloids were substantially ordered and highly divaricated after incubation with both OASL and ZBP1 (Fig. 5d and Extended Data Fig. 5f, g). Time-dependent and interaction-dependent amyloidogenesis of RIPK3₂₉₅₋₅₁₈ was noted by the growth of RIPK3₂₉₅₋₅₁₈

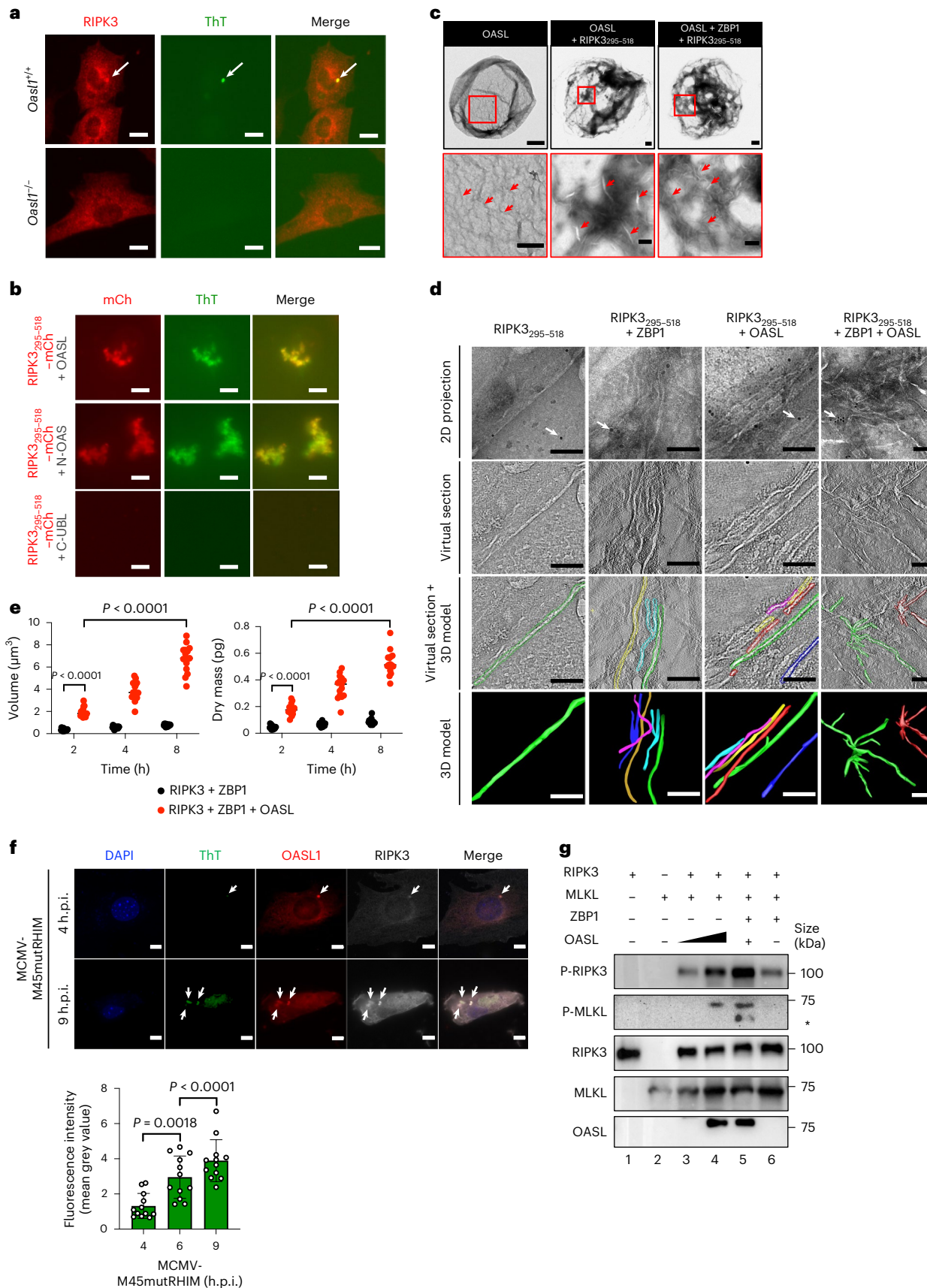
Fig. 5 | OASL phase condensates nucleate RIPK3 and promote RIPK3 activation and amyloid formation.

a, *Oas1l*^{+/+} and *Oas1l*^{-/-} primary fibroblasts infected with MCMV-M45mutRHIM and immunostained for endogenous RIPK3 (anti-RIPK3) and amyloid-like structure (ThT). Arrow indicates foci positive for RIPK3 and ThT. **b**, Filamentous structure formation after mixing RIPK3₂₉₅₋₅₁₈-mCherry with high concentrations (2.5 μ M) of purified OASL, N-OAS or C-UBL. **c**, Top: TEM images of OASL-GFP alone, with RIPK3₂₉₅₋₅₁₈-mCherry or with RIPK3₂₉₅₋₅₁₈-mCherry and ZBP1-BFP after phase-separation induction for 2 h. Bottom: magnified images of the red square area for each image showing fibril-like structures (red arrows) inside the OASL droplet. **d**, Electron tomogram of RIPK3₂₉₅₋₅₁₈-mCherry amyloids alone, with ZBP1-BFP, OASL-GFP, or with ZBP1-BFP and OASL-GFP. First row: 2D projections of the amyloid fibrils. Arrows indicate gold particles used for image alignment. Second row: virtual sections through the tomogram at different z axis positions. Third row: overlay of virtual sections and 3D models. Fourth row: reconstructed 3D model of the

amyloid fibrils. **e**, Quantitative analysis of 3D tomograms of RIPK3-mCherry after incubation with ZBP1 or with ZBP1 and OASL at the indicated times ($n = 15$). **f**, Top: *Oas1l*^{-/-} fibroblasts reconstituted with OASL1-mCherry, infected with MCMV-M45mutRHIM and immunostained for amyloid-like structures. Arrows indicate foci positive for OASL1, RIPK3 and ThT. Bottom: quantification of ThT mean fluorescence intensity per time point ($n = 12$). **g**, In vitro kinase reactions of purified OASL-GFP, GST-RIPK3, ZBP1-BFP and MLKL. OASL-RIPK3-ZBP1 were induced for phase separation, subjected to kinase reaction and immunoblotted for Ser227 autophosphorylation of RIPK3 and Ser358 phosphorylation of MLKL (asterisk indicates a nonspecific band). Data are representative of three (**a, b, e-g**) independent experiments, with similar results obtained. For **c, d**, TEM images are representative of at least eight fields with four independent experiments. For **e, f**, data are presented as the mean \pm s.e.m. and statistical analyses were performed using two-way (**e**) or one-way (**f**) ANOVA. Scale bars, 100 nm (**d**), 200 nm (**c**, bottom), 500 nm (**c**, top) or 10 μ m (**a, b, f**).

fibriils after long in vitro incubation (120 min) compared with short incubation (20 min), especially those formed by RIPK3₂₉₅₋₅₁₈ alone (Extended Data Fig. 5h). Holotomography imaging also revealed that

RIPK3 increasingly nucleated over time as OASL droplets grew in size and concentration in vitro. This RIPK3 nucleation was not observed after incubation with ZBP1 alone (Fig. 5e and Extended Data Fig. 5i–k),



which highlights the role of OASL phase condensation in nucleating RIPK3 and promoting RIPK3 amyloid fibril formation. The growth and maturation of RIPK3 amyloid-like fibrils within the OASL droplets were further evidenced in MCMV-M45mutRHIM-infected primary fibroblasts by the colocalization of ThT-positive OASL and RIPK3 foci and the increasing ThT signal over time (Fig. 5f).

To further demonstrate that fibrils of and activated RIPK3 directly transduce downstream signalling to its substrate MLKL, an *in vitro* kinase reaction was performed after induction of phase separation of OASL, RIPK3 and ZBP1 followed by the addition of MLKL and ATP to induce the kinase reaction. OASL phase separation regulated RIPK3 autophosphorylation, which subsequently induced MLKL phosphorylation (Fig. 5g). However, the RHIM-mediated interaction between RIPK3 and ZBP1 was not sufficient for inducing RIPK3 amyloid fibril formation and MLKL phosphorylation without OASL (Fig. 5d,e,g and Extended Data Fig. 5f–k). These data demonstrate that the recruitment of RIPK3 and ZBP1 into OASL droplets results in pervasive amyloid formation of RIPK3 during virus infection, which indicates that OASL phase condensation is a spatial hub for nucleating RIPK3 to accelerate amyloid fibril formation.

OASL1-mediated necroptosis restricts MCMV replication and inflammation *in vivo*

To further determine the role of OASL1 in virus-induced necroptotic cell death *in vivo*, we infected age-matched and sex-matched *Oas1l^{+/+}* and *Oas1l^{-/-}* littermate mice with either MCMV-WT or MCMV-M45mutRHIM via footpad injection and monitored footpad swelling for up to 12 days post infection (d.p.i.) (Fig. 6a,b). As previously described^{5,6}, footpad swelling in MCMV-WT-infected *Oas1l^{+/+}* mice peaked at 6 d.p.i. (Fig. 6a), whereas it was apparently reduced in MCMV-M45mutRHIM-infected *Oas1l^{+/+}* mice (Fig. 6b). By contrast, *Oas1l^{-/-}* mice exhibited reduced footpad swelling upon either MCMV-WT or MCMV-M45mutRHIM infection compared with *Oas1l^{+/+}* littermates (Fig. 6a,b). Although *Ripk3^{-/-}* mice exhibited slightly reduced footpad swelling than WT mice upon MCMV-WT infection, they showed peak footpad swelling at 6 d.p.i. upon either MCMV-WT or MCMV-M45mutRHIM infection (Extended Data Fig. 6a,b). None of the infected mice exhibited lethality or significant body weight changes following either MCMV-WT or MCMV-M45mutRHIM infection (Extended Data Fig. 6b,c).

Previously, it has been reported that MCMV can be disseminated from the initial footpad inoculation site to the distal organ salivary glands (SGs) to establish persistent infection⁵⁸. MCMV-WT viral titres in SGs were comparable between *Oas1l^{+/+}* and *Oas1l^{-/-}* mice at 6 d.p.i. (Extended Data Fig. 6d), but were significantly higher in *Oas1l^{-/-}* mice than in *Oas1l^{+/+}* mice at 12 d.p.i. (Fig. 6c). Notably, the dissemination of MCMV-M45mutRHIM into SGs was detected in *Oas1l^{-/-}* mice as early as 2 d.p.i. (Extended Data Fig. 6e), and their titres were considerably higher in *Oas1l^{-/-}* mice than in *Oas1l^{+/+}* mice at 12 d.p.i. (Fig. 6c). These results demonstrate that OASL1-mediated necroptosis restricts MCMV replication and dissemination.

Fig. 6 | OASL1-mediated necroptosis restricts MCMV viral replication and inflammation *in vivo*. a, b, Time course measurement of footpad swelling

caused by subcutaneous footpad injection of age-matched and sex-matched *Oas1l^{+/+}* and *Oas1l^{-/-}* mice with 10^6 p.f.u. MCMV-WT (a) (*Oas1l^{+/+}*, $n = 8$; *Oas1l^{-/-}*, $n = 6$ for 0–10 d.p.i., $n = 2$ for 12 d.p.i.) or MCMV-M45mutRHIM (b) (*Oas1l^{+/+}*, $n = 8$ for 0–6 d.p.i., $n = 4$ for 8–12 d.p.i.; *Oas1l^{-/-}*, $n = 8$, except $n = 2$ for 6 d.p.i.). The thickness of the footpads was measured using a digital caliper. Data are presented as the percent increase in thickness relative to the pre-injection measurement and plotted as mean values at the indicated times ($n = 9$ mice per genotype). c, Virus titres in SGs of *Oas1l^{+/+}* and *Oas1l^{-/-}* mice at 12 d.p.i. of MCMV-WT or MCMV-M45mutRHIM were determined by plaque assay. $\log_{10}(2)$ is the limit of detection owing to the toxicity of SG homogenates in NIH3T3 cells ($n = 3$ mice per genotype). d, IL-1 α levels in the serum of *Oas1l^{+/+}* and *Oas1l^{-/-}* mice at 12 d.p.i. of MCMV-WT or MCMV-M45mutRHIM were determined by ELISA

As a consequence of necroptosis, levels of released interleukin-1 α (IL-1 α) in the serum were considerably higher in *Oas1l^{+/+}* mice infected with either MCMV-WT or MCMV-M45mutRHIM compared with those in *Oas1l^{-/-}* mice (Fig. 6d and Extended Data Fig. 6f). Consistent with the reduced footpad swelling and serum IL-1 α levels, MCMV-WT-infected or M45mutRHIM-infected *Oas1l^{-/-}* mice showed a marked reduction in immune cell infiltration and epidermal hyperplasia (Fig. 6e and Extended Data Fig. 6g,h). Indeed, immunohistochemistry of virus-infected mouse footpads showed intense phospho-RIPK3 and phospho-MLKL signals in the dermis region of the footpads from MCMV-WT-infected or MCMV-M45mutRHIM-infected *Oas1l^{+/+}* mice, whereas the signals were substantially reduced in *Oas1l^{-/-}* mice (Fig. 6f,g), which suggests that OASL1 positively regulates RIPK3 and MLKL activation. Collectively, the markedly reduced activation of the key necroptotic kinase RIPK3 and the effector MLKL upon virus infection in *Oas1l^{-/-}* mice suggests that OASL1 has a pivotal role in the execution of necroptosis *in vivo* to restrict MCMV replication and elicit antiviral inflammatory responses.

OASL1-driven necroptosis promotes antiviral activity during other viral infections

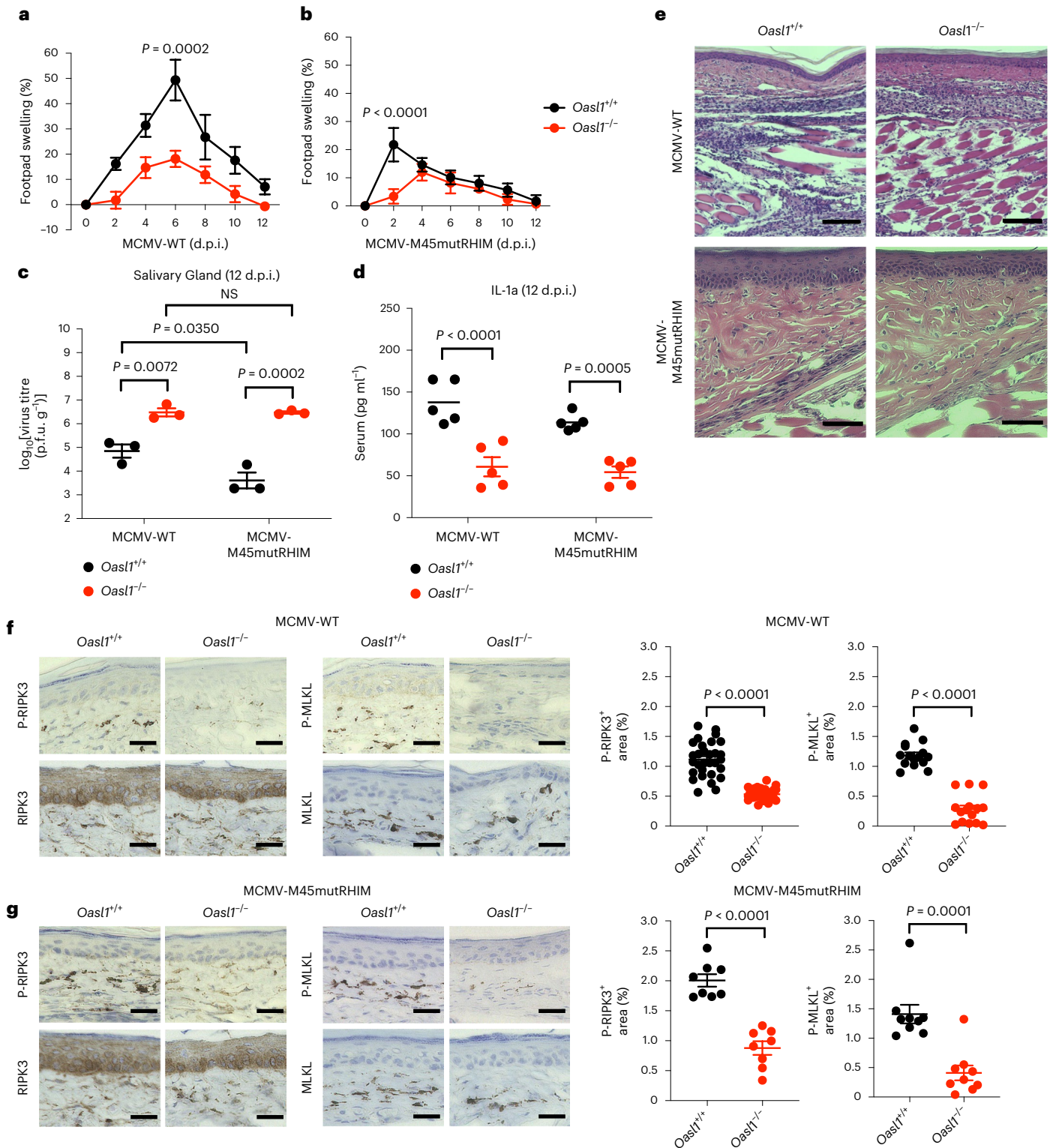
The *in vivo* role of OASL1 in virus-induced necroptosis was further tested for HSV-1 and IAV infection, both of which are known to induce RIPK3-mediated necroptosis^{7–9,42,59}. *Oas1l^{+/+}* and *Oas1l^{-/-}* mice were intraperitoneally infected with 10^7 plaque-forming units (p.f.u.) of the HSV-1 KOS strain (Fig. 7a–c) or intranasally infected with a sublethal dose of 10^2 p.f.u. of the mouse-adapted IAV A/PR/8/H1N1 strain (Fig. 7d–g). Upon HSV-1 infection, *Oas1l^{-/-}* mice showed considerable weight loss compared with *Oas1l^{+/+}* mice, with the most significant reduction observed at 6 d.p.i. (Fig. 7a). Consistently, *Oas1l^{-/-}* mice showed significantly higher HSV-1 DNA copy number and markedly lower serum IL-1 α level compared with *Oas1l^{+/+}* mice (Fig. 7b,c). Around 70% (10 out of 14) of *Oas1l^{-/-}* mice died from the sublethal dose of IAV infection, whereas only 9% (1 out of 11) of *Oas1l^{+/+}* littermate mice died (Fig. 7d). Similar to HSV-1 infection, more significant weight loss was observed in IAV-infected *Oas1l^{-/-}* mice compared with *Oas1l^{+/+}* mice, with higher peak weight loss between 6 and 8 d.p.i. (Fig. 7e). Furthermore, measuring progeny IAV production in the lungs showed 10-fold to 100-fold higher IAV titres in *Oas1l^{-/-}* mice compared with *Oas1l^{+/+}* mice at 7 d.p.i. (Fig. 7f). This result highlighted a correlation between mortality and greater body weight loss and higher virus burden. IAV-infected *Oas1l^{-/-}* mice also showed alleviated pulmonary inflammation and lower serum IL-1 α levels compared with IAV-infected *Oas1l^{+/+}* littermate mice (Fig. 7g and Extended Data Fig. 7a–d). Notably, similar phenotypes have been observed when *Ripk3^{-/-}* mice are infected with MCMV-WT, MCMV-M45mutRHIM, HSV-1 or IAV^{5,7,9,42}. Overall, these results show that OASL1 induces necroptosis to promote antiviral inflammation and consequently restricts viral replication and pathogenesis.

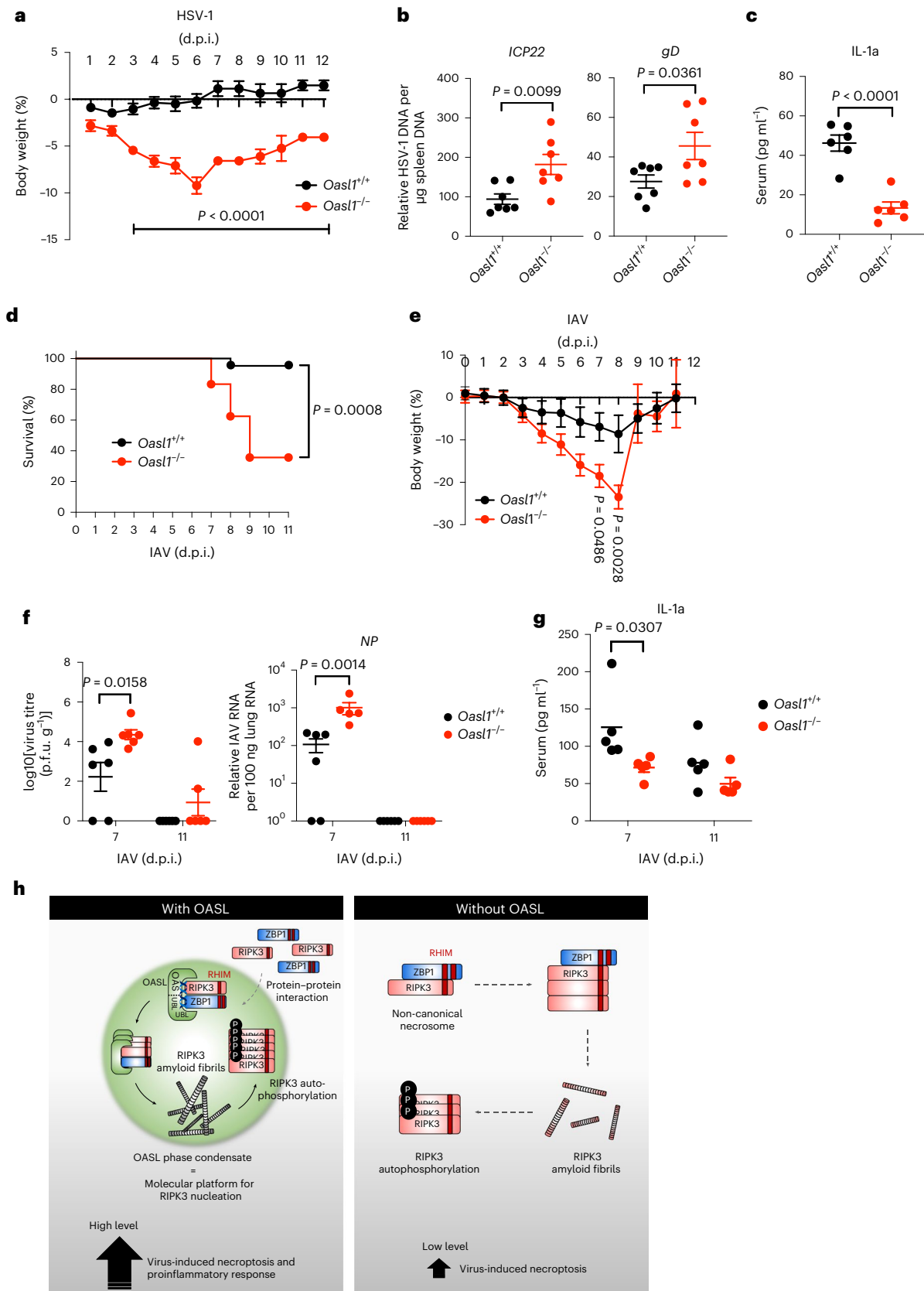
($n = 5$ mice per genotype). e, Haematoxylin and eosin staining for histological analysis of footpads from mice infected with MCMV-WT (day 6) or MCMV-M45mutRHIM (day 2). f, g, Left: footpad sections corresponding to e (MCMV-WT (f) and MCMV-M45mutRHIM (g)) were subjected to immunohistochemistry staining of RIPK3, P-RIPK3, MLKL and P-MLKL. Positive staining appears brown with haematoxylin counterstain. Right: quantification of the areas stained by P-RIPK3 and P-MLKL in mice infected with MCMV-WT (f, $n = 30$ for P-RIPK3, $n = 15$ for P-MLKL) or MCMV-M45mutRHIM (g, $n = 8$ for P-RIPK3, $n = 9$ for P-MLKL) in mouse footpads with the indicated genotypes using ImageJ (Fiji) software. All data are pooled from three independent experiments. For a–d, f, g, data are presented as the mean \pm s.e.m. Statistical analyses were performed using two-tailed unpaired *t*-test (f, g) or two-way ANOVA (a–d). Scale bars, 20 μ m (f, g) or 50 μ m (e).

Discussion

Robust activation of necroptosis during virus infection requires contemporaneous engagement of intact TNF and type I IFN signalling, which suggests that there is a node of pathway crosstalk between the two signalling pathways. Here we demonstrated that the IFN-inducible protein OASL is a previously undescribed component of the non-canonical necrosome complex that governs a sequential event during virus-induced necroptosis. Our study revealed that OASL undergoes dsRNA-dependent LLPS, which serves as a

scaffold to facilitate the assembly of the RIPK3–ZBP1 necrosome during virus infection. These OASL liquid droplets effectively recruit RIPK3 and ZBP1, providing a spatially partitioned platform for the amyloidogenic protein RIPK3 to nucleate and induce amyloid fibril formation and prompt activation during immediate challenges (Fig. 7h). Subsequently, activated RIPK3 phosphorylates MLKL to execute high levels of virus-induced necroptosis and proinflammatory responses. A rigorous structural study is needed to further characterize the formation, as well as its functionality





as molecular platforms, of the RIPK3 amyloid fibrils during virus-induced necroptosis.

Biomolecular condensates formed by LLPS through multivalent protein–nucleic acid interactions enable spatially segregated molecular platforms to fine-tune intricate biological signalling. The physical

properties of droplet-like phase separation of RNA-binding proteins is not solely dependent on the negative charge of its target RNAs^{60,61}. We found that OASL formed larger phase-separated condensates following treatment with poly(I:C) HMW than with poly(I:C) LMW in vitro, which implies that the length of dsRNA, and hence the multivalency,

Fig. 7 | OASL1-driven necroptosis promotes antiviral activity during other viral infections. **a**, Body weight changes of age-matched and sex-matched *OasL1^{+/+}* ($n = 8$ for 0–6 d.p.i., $n = 4$ for 7–12 d.p.i.) and *OasL1^{-/-}* ($n = 6$ for 0–6 d.p.i., $n = 2$ for 7–8 d.p.i., $n = 4$ for 9–12 d.p.i.) littermate mice after intraperitoneal injection of 10^7 p.f.u. of the HSV-1 strain KOS. **b**, Viral DNA in spleens from HSV-1-infected *OasL1^{+/+}* and *OasL1^{-/-}* littermate mice were determined by genomic DNA quantitative PCR ($n = 7$ mice per genotype). Data were normalized against a host housekeeping gene. **c**, IL-1 α levels in the sera of *OasL1^{+/+}* and *OasL1^{-/-}* mice infected with HSV-1 were determined by ELISA ($n = 5$ mice per genotype). **d**, Survival analysis of age-matched and sex-matched *OasL1^{+/+}* and *OasL1^{-/-}* littermate mice intranasally infected with 100 p.f.u. of the IAV strain PR8 ($n = 11$ for *OasL1^{+/+}*, $n = 14$ for *OasL1^{-/-}*). **e**, Body weight changes of mice (*OasL1^{+/+}*, $n = 10$ for 0–6 d.p.i., $n = 6$ for 7–9 d.p.i., $n = 3$ for 10–11 d.p.i.; *OasL1^{-/-}*, $n = 14$ for 0–6 d.p.i., $n = 11$ for 7–8 d.p.i., $n = 2$ for 9–11 d.p.i.) in **d**, **f**, Virus titres and viral RNA loads in

lungs from IAV-infected *OasL1^{+/+}* and *OasL1^{-/-}* littermate mice were determined by plaque assay (left) and quantitative PCR with reverse transcription (right) ($n = 6$ mice per genotype). **g**, IL-1 α levels in the sera of *OasL1^{+/+}* and *OasL1^{-/-}* mice infected with IAV were determined by ELISA ($n = 5$ mice per genotype). All data are pooled from two independent experiments. For **a–c**, **e–g**, data are presented as the mean \pm s.e.m. Statistical analyses were performed using two-tailed unpaired *t*-test (**b**, **c**) or two-way ANOVA (**a**, **e–g**). Data for **d** are presented as a Kaplan–Meier plot. For **b**, **c** and **f**, **g**, each symbol represents one mouse, and horizontal lines represent the mean value. **h**, Representative model of OASL-mediated virus-induced necroptosis. OASL undergoes LLPS and recruits RIPK3 and ZBP1 via protein–protein interactions to scaffold the assembly. OASL phase condensation induces RIPK3 nucleation and amyloid-like fibril formation, which in turn leads to RIPK3 autophosphorylation. Consequently, activated RIPK3 induces high levels of necroptosis and proinflammatory responses during virus-induced necroptosis.

could be an important factor that determines the magnitude of OASL droplet formation⁶¹. Likewise, the availability of cytosolic viral dsRNA during virus infection may determine the duration and frequency of OASL LLPS. The identification of specific target dsRNA in the future can provide insights into our understanding of not only how the assembly of OASL is spatially patterned with viral dsRNA but also what secondary structure of target RNAs may trigger the necroptotic activity of OASL⁶⁰.

Although RIPK3 is not able to undergo phase separation on its own, it has been reported that RIPK3 can heterocomplex with its RHIM-containing adaptor molecules, RIPK1 or ZBP1, to form amyloid-like structures in vitro, ultimately forming an energetically favourable conformation¹⁸. These RHIM–RHIM hetero-amyloids display high energetic preference over RIPK3 homo-amyloids, thereby implicating RIPK3 hetero-amyloids for a broader range of signalling activities before the formation of homo-amyloids¹⁹. These findings collectively suggest that an efficient assembly of higher-order signalling platforms, such as amyloid-like fibrous structures, often requires scaffolding molecules that facilitate the polymerization of subunits to become energetically favourable and consequently execute condition-specific signals. Here we showcased OASL liquid droplets that serve as a molecular platform to provide a spatial segregation region for RIPK3 to induce polymerization and amyloid-like fibril formation. Our model suggests that the OASL–RIPK3 interaction enhances the formation of the RIPK3 amyloid-like fibril signalling complex, which prolongs RIPK3 activation and drives high levels of MLKL phosphorylation, ultimately inducing robust necroptosis during virus infection. As OASL nucleates RIPK3, together with ZBP1 via RHIM-mediated interactions, within its liquid droplet, stronger intermolecular and intramolecular interactions within the droplets may allow RIPK3 to promptly achieve the minimal binding proximity and concentration for homo-oligomerization, triggering the formation of amyloid fibrils. These polymeric platforms may then exert augmented forces to trigger efficient signal transduction activity. Indeed, higher-order assemblies like amyloid fibrils have gained attention as a platform to induce signal transduction, such as apoptosis-associated spec-like protein (ASC)-dependent inflammasome assembly or FAS-associated death domain protein (FADD) and caspase-8 in apoptosis^{62,63}. In-depth study of the structural perspectives of OASL liquid phase condensates is needed to elucidate how this RIPK3–ZBP1–OASL necrosome regulates condition-specific signal transduction activity.

In summary, this study elucidated a previously uncharacterized mechanism of RIPK3 activation during virus-induced necroptosis and identified a vital role of the IFN-inducible protein OASL in exploiting phase separation to activate executioner signals by scaffolding the assembly of RIPK3 and ZBP1. OASL-mediated necroptosis is an effector pathway of the IFN-mediated antiviral response that reduces virus burden by initiating proinflammatory cell death: necroptosis. This pathway is functionally distinct from the previously described role of the OAS

protein family in the 2-5A synthetase-directed RNase L pathway as well as the role of OASL in IFN production. Although OASL has been implicated in differential aspects of antiviral immunity, herein we described an antiviral mechanism of OASL by defining the biochemical characteristics of OASL. This crucial role of OASL in the crosstalk between the OAS family proteins and necroptosis brings insights into our understanding of its function as a regulator of necroptosis-mediated inflammatory response to combat pathogenic challenges.

Online content

Any methods, additional references, Nature Portfolio reporting summaries, source data, extended data, supplementary information, acknowledgements, peer review information; details of author contributions and competing interests; and statements of data and code availability are available at <https://doi.org/10.1038/s41556-022-01039-y>.

References

- Pasparakis, M. & Vandenabeele, P. Necroptosis and its role in inflammation. *Nature* **517**, 311–320 (2015).
- Cho, Y. S. et al. Phosphorylation-driven assembly of the RIP1–RIP3 complex regulates programmed necrosis and virus-induced inflammation. *Cell* **137**, 1112–1123 (2009).
- Zhang, D. W. et al. RIP3, an energy metabolism regulator that switches TNF-induced cell death from apoptosis to necrosis. *Science* **325**, 332–336 (2009).
- Mocarski, E. S., Upton, J. W. & Kaiser, W. J. Viral infection and the evolution of caspase 8-regulated apoptotic and necrotic death pathways. *Nat. Rev. Immunol.* **12**, 79–88 (2011).
- Upton, J. W., Kaiser, W. J. & Mocarski, E. S. Virus inhibition of RIP3-dependent necrosis. *Cell Host Microbe* **7**, 302–313 (2010).
- Upton, J. W., Kaiser, W. J. & Mocarski, E. S. DAI/ZBP1/DLM-1 complexes with RIP3 to mediate virus-induced programmed necrosis that is targeted by murine cytomegalovirus vIRA. *Cell Host Microbe* **11**, 290–297 (2012).
- Huang, Z. et al. RIP1/RIP3 binding to HSV-1 ICP6 initiates necroptosis to restrict virus propagation in mice. *Cell Host Microbe* **17**, 229–242 (2015).
- Guo, H. et al. Species-independent contribution of ZBP1/DAI/DLM-1-triggered necroptosis in host defense against HSV1. *Cell Death Dis.* **9**, 816 (2018).
- Nogusa, S. et al. RIPK3 activates parallel pathways of MLKL-driven necroptosis and FADD-mediated apoptosis to protect against influenza A virus. *Cell Host Microbe* **20**, 13–24 (2016).
- Grootjans, S., Vanden Berghe, T. & Vandenabeele, P. Initiation and execution mechanisms of necroptosis: an overview. *Cell Death Differ.* **24**, 1184–1195 (2017).
- Nailwal, H. & Chan, F. K. Necroptosis in anti-viral inflammation. *Cell Death Differ.* **26**, 4–13 (2019).

12. Murphy, J. M. et al. The pseudokinase MLKL mediates necroptosis via a molecular switch mechanism. *Immunity* **39**, 443–453 (2013).
13. Cai, Z. et al. Plasma membrane translocation of trimerized MLKL protein is required for TNF-induced necroptosis. *Nat. Cell Biol.* **16**, 55–65 (2014).
14. Dondelinger, Y. et al. MLKL compromises plasma membrane integrity by binding to phosphatidylinositol phosphates. *Cell Rep.* **7**, 971–981 (2014).
15. Wang, H. et al. Mixed lineage kinase domain-like protein MLKL causes necrotic membrane disruption upon phosphorylation by RIP3. *Mol. Cell* **54**, 133–146 (2014).
16. Kaczmarek, A., Vandennabeele, P. & Krysko, D. V. Necroptosis: the release of damage-associated molecular patterns and its physiological relevance. *Immunity* **38**, 209–223 (2013).
17. Kono, H. & Rock, K. L. How dying cells alert the immune system to danger. *Nat. Rev. Immunol.* **8**, 279–289 (2008).
18. Li, J. et al. The RIP1/RIP3 necrosome forms a functional amyloid signaling complex required for programmed necrosis. *Cell* **150**, 339–350 (2012).
19. Mompean, M. et al. The structure of the necrosome RIPK1–RIPK3 core, a human hetero-amyloid signaling complex. *Cell* **173**, 1244–1253.e10 (2018).
20. Pham, C. L. et al. Viral M45 and necroptosis-associated proteins form heteromeric amyloid assemblies. *EMBO Rep.* <https://doi.org/10.15252/embr.201846518> (2019).
21. Hu, H. et al. RIP3-mediated necroptosis is regulated by inter-filament assembly of RIP homotypic interaction motif. *Cell Death Differ.* **28**, 251–266 (2021).
22. Cook, W. D. et al. RIPK1- and RIPK3-induced cell death mode is determined by target availability. *Cell Death Differ.* **21**, 1600–1612 (2014).
23. Orozco, S. et al. RIPK1 both positively and negatively regulates RIPK3 oligomerization and necroptosis. *Cell Death Differ.* **21**, 1511–1521 (2014).
24. Wu, X. N. et al. Distinct roles of RIP1–RIP3 hetero- and RIP3–RIP3 homo-interaction in mediating necroptosis. *Cell Death Differ.* **21**, 1709–1720 (2014).
25. Sun, L. et al. Mixed lineage kinase domain-like protein mediates necrosis signaling downstream of RIP3 kinase. *Cell* **148**, 213–227 (2012).
26. Weber, K., Roelandt, R., Bruggeman, I., Estornes, Y. & Vandennabeele, P. Nuclear RIPK3 and MLKL contribute to cytosolic necrosome formation and necroptosis. *Commun. Biol.* **1**, 6 (2018).
27. Dillon, C. P. et al. RIPK1 blocks early postnatal lethality mediated by caspase-8 and RIPK3. *Cell* **157**, 1189–1202 (2014).
28. Silke, J., Rickard, J. A. & Gerlic, M. The diverse role of RIP kinases in necroptosis and inflammation. *Nat. Immunol.* **16**, 689–697 (2015).
29. Schoggins, J. W. & Rice, C. M. Interferon-stimulated genes and their antiviral effector functions. *Curr. Opin. Virol.* **1**, 519–525 (2011).
30. Schoggins, J. W. et al. Pan-viral specificity of IFN-induced genes reveals new roles for cGAS in innate immunity. *Nature* **505**, 691–695 (2014).
31. Ghosh, A. et al. Oligoadenylate-synthetase-family protein OASL inhibits activity of the DNA sensor cGAS during DNA virus infection to limit interferon production. *Immunity* **50**, 51–63.e5 (2019).
32. Zhu, J. et al. Antiviral activity of human OASL protein is mediated by enhancing signaling of the RIG-I RNA sensor. *Immunity* **40**, 936–948 (2014).
33. Banani, S. F., Lee, H. O., Hyman, A. A. & Rosen, M. K. Biomolecular condensates: organizers of cellular biochemistry. *Nat. Rev. Mol. Cell Biol.* **18**, 285–298 (2017).
34. Bergeron-Sandoval, L. P., Safaee, N. & Michnick, S. W. Mechanisms and consequences of macromolecular phase separation. *Cell* **165**, 1067–1079 (2016).
35. Yu, X. et al. The STING phase-separator suppresses innate immune signalling. *Nat. Cell Biol.* **23**, 330–340 (2021).
36. Andreeva, L. & Wu, H. STING condensates on ER limit IFN response. *Nat. Cell Biol.* **23**, 299–300 (2021).
37. Lin, Y., Protter, D. S., Rosen, M. K. & Parker, R. Formation and maturation of phase-separated liquid droplets by RNA-binding proteins. *Mol. Cell* **60**, 208–219 (2015).
38. Patel, A. et al. A liquid-to-solid phase transition of the ALS protein FUS accelerated by disease mutation. *Cell* **162**, 1066–1077 (2015).
39. Ray, S. et al. α -Synuclein aggregation nucleates through liquid–liquid phase separation. *Nat. Chem.* **12**, 705–716 (2020).
40. He, S. et al. Receptor interacting protein kinase-3 determines cell necrotic response TNF- α . *Cell* **137**, 1100–1111 (2009).
41. Kuriakose, T. et al. ZBP1/DAI is an innate sensor of influenza virus triggering the NLRP3 inflammasome and programmed cell death pathways. *Sci. Immunol.* <https://doi.org/10.1126/sciimmunol.aag2045> (2016).
42. Thapa, R. J. et al. DAI senses influenza A virus genomic RNA and activates RIPK3-dependent cell death. *Cell Host Microbe* **20**, 674–681 (2016).
43. Jiao, H. et al. Z-nucleic-acid sensing triggers ZBP1-dependent necroptosis and inflammation. *Nature* **580**, 391–395 (2020).
44. Zhang, T. et al. Influenza virus Z-RNAs induce ZBP1-mediated necroptosis. *Cell* **180**, 1115–1129.e13 (2020).
45. Fonin, A. V., Darling, A. L., Kuznetsova, I. M., Turoverov, K. K. & Uversky, V. N. Intrinsically disordered proteins in crowded milieu: when chaos prevails within the cellular gumbo. *Cell. Mol. Life Sci.* **75**, 3907–3929 (2018).
46. Romero, P. et al. Sequence complexity of disordered protein. *Proteins* **42**, 38–48 (2001).
47. Kroschwald, S. et al. Promiscuous interactions and protein disaggregases determine the material state of stress-inducible RNP granules. *eLife* **4**, e06807 (2015).
48. Peskett, T. R. et al. A liquid to solid phase transition underlying pathological huntingtin exon1 aggregation. *Mol. Cell* **70**, 588–601.e6 (2018).
49. Du, M. & Chen, Z. J. DNA-induced liquid phase condensation of cGAS activates innate immune signaling. *Science* **361**, 704–709 (2018).
50. Rayman, J. B., Karl, K. A. & Kandel, E. R. TIA-1 self-multimerization, phase separation, and recruitment into stress granules are dynamically regulated by Zn²⁺. *Cell Rep.* **22**, 59–71 (2018).
51. Alberti, S., Gladfelter, A. & Mittag, T. Considerations and challenges in studying liquid–liquid phase separation and biomolecular condensates. *Cell* **176**, 419–434 (2019).
52. Jung, J. et al. Label-free non-invasive quantitative measurement of lipid contents in individual microalgal cells using refractive index tomography. *Sci. Rep.* **8**, 6524 (2018).
53. Ibsen, M. S. et al. Structural and functional analysis reveals that human OASL binds dsRNA to enhance RIG-I signaling. *Nucleic Acids Res.* **43**, 5236–5248 (2015).
54. Weber, F., Wagner, V., Rasmussen, S. B., Hartmann, R. & Paludan, S. R. Double-stranded RNA is produced by positive-strand RNA viruses and DNA viruses but not in detectable amounts by negative-strand RNA viruses. *J. Virol.* **80**, 5059–5064 (2006).
55. Voros, J. The density and refractive index of adsorbing protein layers. *Biophys. J.* **87**, 553–561 (2004).
56. Alberti, S. & Dormann, D. Liquid–liquid phase separation in disease. *Annu. Rev. Genet.* **53**, 171–194 (2019).
57. Molliex, A. et al. Phase separation by low complexity domains promotes stress granule assembly and drives pathological fibrillization. *Cell* **163**, 123–133 (2015).

58. Stoddart, C. A. et al. Peripheral blood mononuclear phagocytes mediate dissemination of murine cytomegalovirus. *J. Virol.* **68**, 6243–6253 (1994).
59. Wang, X. et al. Direct activation of RIP3/MLKL-dependent necrosis by herpes simplex virus 1 (HSV-1) protein ICP6 triggers host antiviral defense. *Proc. Natl Acad. Sci. USA* **111**, 15438–15443 (2014).
60. Langdon, E. M. et al. mRNA structure determines specificity of a polyQ-driven phase separation. *Science* **360**, 922–927 (2018).
61. Zhang, H. et al. RNA controls polyQ protein phase transitions. *Mol. Cell* **60**, 220–230 (2015).
62. Cai, X. et al. Prion-like polymerization underlies signal transduction in antiviral immune defense and inflammasome activation. *Cell* **156**, 1207–1222 (2014).
63. Siegel, R. M. et al. Death-effector filaments: novel cytoplasmic structures that recruit caspases and trigger apoptosis. *J. Cell Biol.* **141**, 1243–1253 (1998).

Publisher's note Springer Nature remains neutral with regard to jurisdictional claims in published maps and institutional affiliations.

Open Access This article is licensed under a Creative Commons Attribution 4.0 International License, which permits use, sharing, adaptation, distribution and reproduction in any medium or format, as long as you give appropriate credit to the original author(s) and the source, provide a link to the Creative Commons licence, and indicate if changes were made. The images or other third party material in this article are included in the article's Creative Commons licence, unless indicated otherwise in a credit line to the material. If material is not included in the article's Creative Commons licence and your intended use is not permitted by statutory regulation or exceeds the permitted use, you will need to obtain permission directly from the copyright holder. To view a copy of this licence, visit <http://creativecommons.org/licenses/by/4.0/>.

© The Author(s) 2023

Methods

All experiments performed in this study were approved by the Institutional Animal Care and Use Committee and the Institutional Biosafety Committee of the University of Southern California and the Cleveland Clinic.

Primary tail fibroblasts

Primary tail fibroblasts were isolated from tails of 3–4-week-old mice and used for experiments within six passages. In brief, tails were minced and digested with 5 mg ml⁻¹ STEMxyme 1 collagenase/neutral protease (Dispase, Worthington Biochemical) at 37 °C for 1 h. After transferring to complete DMEM medium for overnight culture, cell debris was filtered through a 70- μ m strainer. Primary fibroblasts were then collected by centrifugation and cultured in DMEM supplemented with 10% FBS and 1% penicillin and streptomycin.

Viruses and virological assays

MCMV-WT and MCMV-M45mutRHIM viruses⁵ were gifts from J. W. Upton (Auburn University). Viruses were propagated, concentrated and titrated by plaque assay in NIH3T3 cells. A tenfold serial dilution of whole SG homogenates were prepared in DMEM containing 2% FBS. Cells were incubated with 1 ml of serially diluted tissue homogenates at 37 °C for 2 h. The HSV-1 strain KOS was propagated and titrated by plaque assay in Vero cells.

Mass spectrometry analysis of RIPK3-interacting proteins

Immunoprecipitation products were separated by SDS-PAGE and fixed overnight before silver staining. Protein bands were excised and sent to the Taplin Biological Mass Spectrometry Facility at Harvard Medical School for protein identification.

Mice

Mice were bred and housed in specific pathogen-free facilities that exclude many pathogenic and adventitious viruses, bacteria and parasites, with controlled temperature (20–26 °C), illumination (10 h light–14 h dark) and humidity (30–70%) at the University of Southern California Animal Research Center at Keck Medical School and the Lerner Research Institute Biological Resources Unit at Cleveland Clinic. *Oasl1*^{-/-} mice were generated using the CRISPR–Cas9 system. For production of single guide RNA (sgRNA), a bicistronic vector expressing Cas9 and sgRNA⁶⁴ were digested with BsmBI, and the linearized vector was gel-purified. A pair of oligonucleotides for target exon 2 of the mouse *Oasl1* gene (Supplementary Fig. 1a) was annealed, phosphorylated and ligated into the linearized vector. The T7 promoter was then added to the sgRNA template by PCR amplification. The gel-purified T7-sgRNA PCR product was used as the template for in vitro transcription using a MEGAshortscript T7 kit (Life Technologies). The product was subsequently purified using a MEGAclean kit (Life Technologies) and eluted in RNase-free water. Microinjection of the oligonucleotides was performed at the University of Southern California transgenic/knockout rodent core facility. In brief, *cas9* mRNA (TriLink) and sgRNA were mixed and injected into pronuclei-stage zygotes obtained from embryo donor C57BL/6 female mice. The injected zygotes were transferred into the uterus of pseudopregnant B6D2F1 (C57BL/6 \times DBA2) foster female mice. For genotyping of pups, genomic DNA was extracted from the tail, and the sgRNA target site was PCR-amplified using the following primers: forward: 5'-CTACCATGACAATAAATCTCC-3'; reverse: 5'-TCTTTAGTAGTTCATTCTGCTC-3'. The PCR products were then subjected to T7E1 assays and Sanger sequencing. The protocols for performing mice studies were reviewed and approved by Institutional Animal Care and Use Committees at the University of Southern California Keck Medical School and the Cleveland Clinic.

Plasmids, lentivirus propagation and transductions

Plasmids expressing 3' V5-tagged mouse OASL1 and OASL2 were produced as previously described³² and provided by S. N. Sarkar (University

of Pittsburgh Cancer Institute). Plasmid expressing HA-tagged human RIPK3 was purchased from Addgene (78804). HA-tagged N-terminal kinase domain (RIPK3_{1–313}) or C-terminal unstructured region (RIPK3_{310–486}) of mouse RIPK3 were generated by PCR using pcDNA3-HA-RIPK3 (Addgene, 78805) as the template and subcloning back to the same pcDNA3 background. Plasmids expressing HA-tagged mouse OASL1 and OASL1-RK mutant were generated by PCR using pcDNA3-OASL1-V5 as the template and subcloning to the lentiviral vector pCDH-MCS-EF1 (System Biosciences). To generate lentivirus, HEK 293T cells were seeded onto 6-well plates and transfected with 0.4 μ g pRev, 0.4 μ g pVSV and 0.8 μ g pGag/Pol of the packaging vectors together with the constructs described above by using Lipofectamine 2000 (Invitrogen) according to the manufacturer's manual. Three days after transfection, the supernatants containing lentiviruses were collected, filtered and stored at -80 °C. Primary fibroblasts were transduced with lentiviral supernatants in the presence of polybrene (8 μ g ml⁻¹) for 48 h and reseeded for further experiments.

Immunoprecipitation and immunoblotting analysis

Cell lysates were prepared in lysis buffer containing 10 mM HEPES pH 7.4, 125 mM KCl and 0.5% NP-40 supplemented with protease inhibitor cocktail without EDTA (Roche), quantified by BCA, separated on SDS-PAGE gels and transferred to polyvinylidene difluoride membranes (Bio-Rad) using a semi-dry transfer system (Bio-Rad). Primary antibody (anti-HA (BioLegend), anti-Flag (Sigma), anti-V5 (Thermo Fisher), anti-ZBP1 (Adipogen), anti-RIPK3 (Cell Signaling Technology), anti-phospho-RIPK3 (Cell Signaling Technology), anti-MLKL (Cell Signaling Technology), anti-phospho-MLKL (Cell Signaling Technology), anti-PKR (Santa Cruz), anti-actin (Santa Cruz) or anti-OASL1 (gifted by M. S. Lee, University of Ulsan College of Medicine, Korea); 1:1,000 dilution) was added and incubated overnight at 4 °C, followed by three washes in 1 \times PBS/0.1% Tween-20 (PBS-T). Secondary antibody (anti-rabbit, anti-mouse, anti-mouse light chain; 1:5,000 dilution) was added and incubated for 1–2 h at room temperature, followed by three washes in PBS-T. Blots were imaged using a Bio-Rad ChemiDoc Touch imaging system. For immunoprecipitation, HEK 293T cells were seeded in a 6-well plate one night before transfection with the indicated plasmids using polyethylenimine. After 48 h, cell lysates were prepared as described above, precleared by incubation with protein A/G agarose beads (Thermo) for 1 h at 4 °C and then incubated with anti-Flag (Sigma), anti-V5 (Sigma), anti-HA (Sigma) or anti-RIPK3 (Santa Cruz) antibody-conjugated beads overnight at 4 °C. After four to six washes with lysis buffer, beads containing immunoprecipitated protein complex were eluted with 2 \times Laemmli sample buffer (Sigma) and subjected to immunoblotting.

Cell death analysis

For kinetic analysis of cell death, primary tail fibroblasts were seeded in 96-well clear-bottomed plates at a density to reach full confluency the next day. After overnight culture at 37 °C, cells were infected with virus at a m.o.i. of 5 for 2 h, washed out and replaced with fresh complete medium supplemented with a cell-membrane-impermeable dye, Sytox Green (0.5 μ M; Thermo Fisher). Fluorescence signals of the cells were read every hour at 485 nm excitation and 535 nm emission wavelengths. Data were averaged from primary fibroblasts that were individually isolated from three to six mice with the same genotype. LDH release was determined using a CytoTox 96 Non-Radioactive Cytotoxicity Assay kit (Promega) according to the manufacturer's manual. For ATP level analysis, CellTiter-Glo assays (Promega) were performed according to the manufacturer's manual. Fluorescence or luminescence was recorded and analysed using a FilterMax F5 multimode microplate reader (Molecular Devices).

Proximity Ligation Assay

PLA was performed according to the manufacturer's instructions (Sigma). Primary tail fibroblasts were seeded at 10,000 cells per well

in an 8-well chamber coverslip. After overnight incubation at 37 °C, cells were infected with MCMV-M45mutRHIM for the indicated times, washed with PBS, fixed with 4% paraformaldehyde for 15 min and permeabilized for 10 min at room temperature. The PLA pair of monoclonal rabbit RIPK3 (Cell Signaling Technology) and monoclonal mouse ZBP1 (Adipogen) antibodies were incubated overnight at 4 °C. Images were captured using a fluorescence microscope (Keyence, BZ-X710 series) and quantified using ImageJ (Fiji) software.

Protein expression and purification

Expression constructs were generated in a pGEX-6p-1 vector to contain a PreScission-cleavable site. eGFP C-terminal fused full-length human OASL, N-OAS and C-UBL; mCherry C-terminal fused full-length human RIPK3 and C-terminal unstructured region (RIPK3_{295–518}); and BFP C-terminal fused full-length human ZBP1 were expressed and purified from *Escherichia coli* strain BL21 DE3 (pLys). *E. coli* harbouring a glutathione *S*-transferase (GST)-tagged plasmid encoding fluorescence-fused human OASL or RIPK3 was induced by adding 0.4 mM IPTG at 16 °C for less than 16 h. Bacteria pellets were collected and lysed in lysis buffer containing 10 mM HEPES (pH 7.4), 450 mM KCl, 1 mg ml⁻¹ zymolyase, 1 mM DTT, 0.1% Triton X-100 and protease inhibitor cocktail without EDTA (Roche) at room temperature for 1 h and at 4 °C for 4 h, followed by centrifugation at 16,000g, 4 °C for 30 min. RNase A (1 mg ml⁻¹) was supplemented in the lysis buffer for human ZBP1–BFP protein purification. Supernatant was collected for overnight purification using glutathione sepharose 4B beads (Cytiva). The GST tag was removed using PreScission protease (GE Healthcare), incubating at 4 °C for 18 h. The protein concentration of the fractions containing fluorescence-tagged proteins were measured by SDS–PAGE with BSA standards.

In vitro phase-separation assay

Purified fluorescence-tagged protein in 450 mM salt buffer was diluted to 125 mM KCl in 10 mM HEPES, pH 7.4, in 96-well plates. The plates were incubated at 37 °C and images were captured at indicated time points after incubation. All phase separation of purified protein was performed in phase-separation buffer (10 mM HEPES, pH 7.4, 125 mM KCl) without adding any crowding reagents. For RIPK3_{295–518}–mCherry and ZBP1–BFP recruitment to OASL–GFP droplets, variant GFP-tagged OASL proteins, mCherry-tagged RIPK3_{295–518} and BFP-tagged ZBP1 were mixed and incubated in 96-well plates at 37 °C for 1 h at the indicated concentrations in the phase-separation buffer. Image acquisition of phase separation was performed using a fluorescence microscope (Keyence, BZ-X710 series) under $\times 20$, $\times 40$ and $\times 60$ 1.49-NA oil-immersion objectives. At least four independent imaging areas were analysed for each condition of each replicate. Data shown are representative of at least three independent experiments across five protein preparations.

In vitro fibril formation assay with ThT measurement

In vitro fibril formation assays were performed as previously described⁶⁵. In brief, 30 μ M ThT (Abcam) was added to the mixtures of 0.5 μ M RIPK3_{295–518}–mCherry with different amounts of purified OASL and incubated at 37 °C for 16 h. ThT binding was excited using a wavelength of 430 nm and evaluated by monitoring the emission fluorescence spectrum at wavelengths from 480 nm to 550 nm.

Electron microscopy and immunogold labelling

A total of 5 μ l of individual or mixtures of OASL–GFP, RIPK3_{295–518}–mCherry and ZBP1–BFP proteins were spotted onto Parafilm, and a carbon–formvar-coated copper grid (200 mesh, Ted Pella) was placed on the surface of the droplet. After 1 min of absorption at room temperature, the sample was wicked off the grid by touching the filter paper. The grids were washed with deionized water three times and stained by floating the grids on a droplet of 2% uranyl acetate. For immunogold labelling, the grids were blocked in 1% BSA in PBS for 10 min, followed by staining with rabbit monoclonal anti-RIPK3 antibody (Cell Signaling

Technology) at 1:100 dilution for 2 h. Next, the grids were washed with 1% BSA in PBS for six times, followed by incubation with secondary antibodies (anti-rabbit conjugated with 6 nm and 10 nm gold particles) for 30 min. The grids were washed with PBS six times, followed by deionized water washing and stained with 2% uranyl acetate. Grids were examined and imaged using a transmission electron microscope (FEI, Tecnai G2 Spirit) at 120 kV operated by the Imaging Core of the Lerner Research Institute at the Cleveland Clinic.

Transmission electron tomography

Carbon–formvar-coated copper grids (200 mesh, Ted Pella) were coated with 0.1% (w/v) poly-L-lysine (Sigma) for 10 min and blotted to remove residual liquid. After drying, the grids were incubated with a droplet of sample for 5 min and subsequently washed with distilled water for 5 s, followed by 2% uranyl acetate staining. Afterwards, the grids were treated with 10 nm gold particles (741957, Sigma Aldrich) in water (1:1) and blotted. Single-axis tilt electron tomography was recorded from -60° to 60° using tilt increments of 2° using a transmission electron microscope (FEI, Tecnai F20) at 200 kV equipped with a $4,096 \times 4,096$ pixel CMOS camera (TemCam-F416, TVIPS). The image stack was generated from tilt images and subjected to tomographic reconstructions using the weighted back-projection algorithm in IMOD (v.4.11.2). The 3D model of amyloids was manually traced from the virtual sections of the tomogram.

In vitro kinase assay

In vitro kinase assays were performed as previously described^{2,25}. Human RIPK3, kinase-dead RIPK3-K50A and phosphorylation-dead RIPK3-S227A mutant proteins were purified from *E. coli* using glutathione sepharose beads. After removing the GST tag, 1 ng of RIPK3 protein was mixed with different amounts of purified human OASL protein (5–50 ng) in kinase reaction buffer (20 mM HEPES, pH 7.4, 1 mM DTT, 20 mM MnCl₂, 20 mM MgCl₂, 1 mM EDTA and 100 μ M ATP) supplemented with phosphatase inhibitor cocktail (Sigma). For RIPK3 and MLKL in vitro kinase assays, OASL–GFP and ZBP1–BFP were purified from *E. coli*, and GST–RIPK3 (Sigma) and MLKL (Cusabio) were commercially purchased. GST–RIPK3 (10 ng), ZBP1 (50 ng) and OASL (50 ng) were subjected to phase separation at 37 °C before kinase reaction with MLKL and the kinase reaction buffer (50 ng). The kinase reaction was performed at 30 °C for 45 min in a total volume of 20 μ l, stopped with 20 μ l of 2 \times Laemmli sample buffer, boiled for 5 min and subjected to immunoblotting analysis with the indicated anti-phospho antibodies.

Immunostaining and confocal microscopy

Primary tail fibroblasts were seeded onto an 8-well chamber slide (Nunc Lab-Tek II Chamber Slide system) for overnight culture at 37 °C and infected with a m.o.i. = 5 of MCMV-M45mutRHIM mutant virus for the indicated times. ThT (25 μ M) was added to cells 1 h before fixation¹⁸. Cells were fixed with 4% paraformaldehyde for 15 min, permeabilized in 0.1% Triton X-100 in PBS for 10 min and blocked with 0.5% BSA in PBS containing 0.1% saponin at room temperature. Cells were then incubated with the indicated antibodies overnight at 4 °C, followed by washing with PBS-T three times at room temperature and incubation with anti-mouse IgG Cascade Blue, anti-mouse IgG Alexa Fluor 568, anti-rabbit IgG Alexa Fluor 488 or anti-rabbit IgG Alexa Fluor 568 (Thermo Fisher) at 1:1,000 dilution. The coverslips were mounted and counterstained using Pro-Long Gold Antifade mountant with 4,6-diamidino-2-phenylindole (DAPI, Thermo Fisher). All images were captured using identical settings on a Nikon laser scanning confocal microscope or a Leica SP8 confocal microscope with a $\times 60$ oil-objective, and processed using Nikon's NIS elements, Leica's LAS X and ImageJ software.

Fluorescent recovery after photobleaching assay

Cellular FRAP experiments were performed using a LSM880 Airyscan microscope at 37 °C in a live-cell imaging chamber. *Oasl1*^{-/-} primary

fibroblasts expressing OASL1–mCherry were grown on glass-bottom dishes (MatTek) overnight to reach the desired density. Cells were then inoculated with MCMV-M45mutRHIM for 2 h. OASL1–mCherry condensates were identified by live-staining with SYTO 45 (Thermo Fisher) 30 min before bleaching and partially photobleaching with 50% laser power using a 560 nm laser. Time-lapse images were acquired with 2-s intervals over 2 min after photobleaching. Images were processed using ImageJ, and FRAP data were fit to a single exponential model using GraphPad Prism. The background intensity was subtracted, and values are reported relative to pre-bleaching time points.

Tomography and analysis of parameters

A commercial optical diffraction tomographic system with modifications for 3D fluorescence imaging (HT-2, Tomocube) was utilized to measure the RI tomograms of individual liquid-like droplets. All morphological and biochemical parameters were quantitatively obtained from RI tomograms, as previously described⁶⁶, using the TomoStudio software.

Infection of mice and organ collection

Oasl1^{+/+} and *Oasl1*^{-/-} mice were anaesthetized with isoflurane, followed by subcutaneous injection of 10⁶ p.f.u. MCMV-WT or MCMV-M45mutRHIM virus into the ventral side of the footpads⁵. Infected mice were observed over a period of 14 days for body weight loss and survival. All experiments were performed with sex-matched mice at 6–8 weeks of age. After euthanasia, organs were collected in PBS and stored at –80 °C until thawed for plaque assays. Experiments involving mice were performed under an approved protocol from the Institutional Animal Care and Use committees at the University of Southern California Keck School of Medicine and Cleveland Clinic.

Histological analysis of mouse tissue

Mouse footpads were collected, fixed in 4% paraformaldehyde for 24 h and transferred to 70% ethanol for storage. Tissue sectioning and immunohistochemistry were performed by the University of Southern California Immunohistochemistry Core facility. In brief, footpads were decalcified in formic acid (Immunocal, StatLab), embedded in paraffin and sectioned at 5 µm thickness. Slides were deparaffinized and either stained with haematoxylin and eosin or antigen-retrieved using retrieval buffer for immunohistochemistry staining. Anti-phospho RIPK3 (Cell Signaling Technology) and anti-phospho MLKL (Cell Signaling Technology) were used for staining. Staining was visualized using streptavidin–HRP (Millipore) and DAB substrate (DAKO and Vector Lab). All immunohistochemistry sections were counterstained with haematoxylin. Images were captured using a bright-field microscope (Keyence, BZ-X710 series). Quantification of phosphorylation signals, epidermatitis or inflamed area were calculated into percentage values (positive signal area versus total area of field of view) on individual footpad cross-sections.

ELISA

Cytokines in serum from animal experiments were quantified using ELISA kits for mouse IL-1α (Invitrogen) according to the manufacturer's protocol.

Statistics and reproducibility

Statistical significance was determined using two-tailed unpaired Student's *t*-test for two component comparisons and one-way analysis of variance (ANOVA) with Tukey's comparison or two-way ANOVA with Bonferroni's comparison for multi-component comparisons in GraphPad Prism v.9.1. Survival curves were generated using the Kaplan–Meier method. Quantification of area was performed using ImageJ (Fiji). All experiments were repeated as indicated in the figure legends with a minimum of two independent replications. The exact

value of *n*, representing the number of mice or samples in the experiments, is indicated in each figure legend. No statistical method was used to predetermine sample sizes. Sample sizes were chosen on the basis of standard practice in the field. Data distribution was assumed to be normal, but was not formally tested. No data were excluded from the analyses. No randomization or blinding was used.

Reporting summary

Further information on research design is available in the Nature Portfolio Reporting Summary linked to this article.

Data availability

The data that support the findings of this study are available from the corresponding author upon reasonable request. Source data are provided with this paper.

References

64. Heckl, D. et al. Generation of mouse models of myeloid malignancy with combinatorial genetic lesions using CRISPR–Cas9 genome editing. *Nat. Biotechnol.* **32**, 941–946 (2014).
65. Kim, H. J. et al. Mutations in prion-like domains in hnRNP2B1 and hnRNP1 cause multisystem proteinopathy and ALS. *Nature* **495**, 467–473 (2013).
66. Kim, G. et al. Measurements of three-dimensional refractive index tomography and membrane deformability of live erythrocytes from *Pelophylax nigromaculatus*. *Sci. Rep.* **8**, 9192 (2018).

Acknowledgements

We thank J. Upton (Auburn University), M. S. Lee (University of Ulsan College of Medicine, Korea), S. Sarkar (University of Pittsburgh Cancer Institute), and J.-H. Ahn (Sungkyunkwan University School of Medicine) for providing reagents; members of the J.U.J. Laboratory for discussion; and Tomocube, Republic of Korea, for providing the 3D fluorescence HT-2 holo-tomographic microscope. This work was partly supported by grant numbers CA200422, CA251275, AI140718, AI140705, AI140705S1, AI152190, AI171201, DE023926, DE028521 and KGM9942011, and a Betsy B. deWindt endowment to J.U.J., grant K99DE028573 to W.C., and grant K99HL153688 to Y.J.C.

Author contributions

S.-A.L., L.-C.C. and J.U.J. designed the experiments, analysed the data, interpreted the results and wrote the manuscript. S.-A.L., L.-C.C., W.J. and D.K. performed the experiments. W.J., D.K., J.W.B., W.C., S.-S.F., Y.J.C., U.Y.C., A.B. and J.-S.Y. contributed to data interpretation and discussion.

Competing interests

The authors declare no competing interests.

Additional information

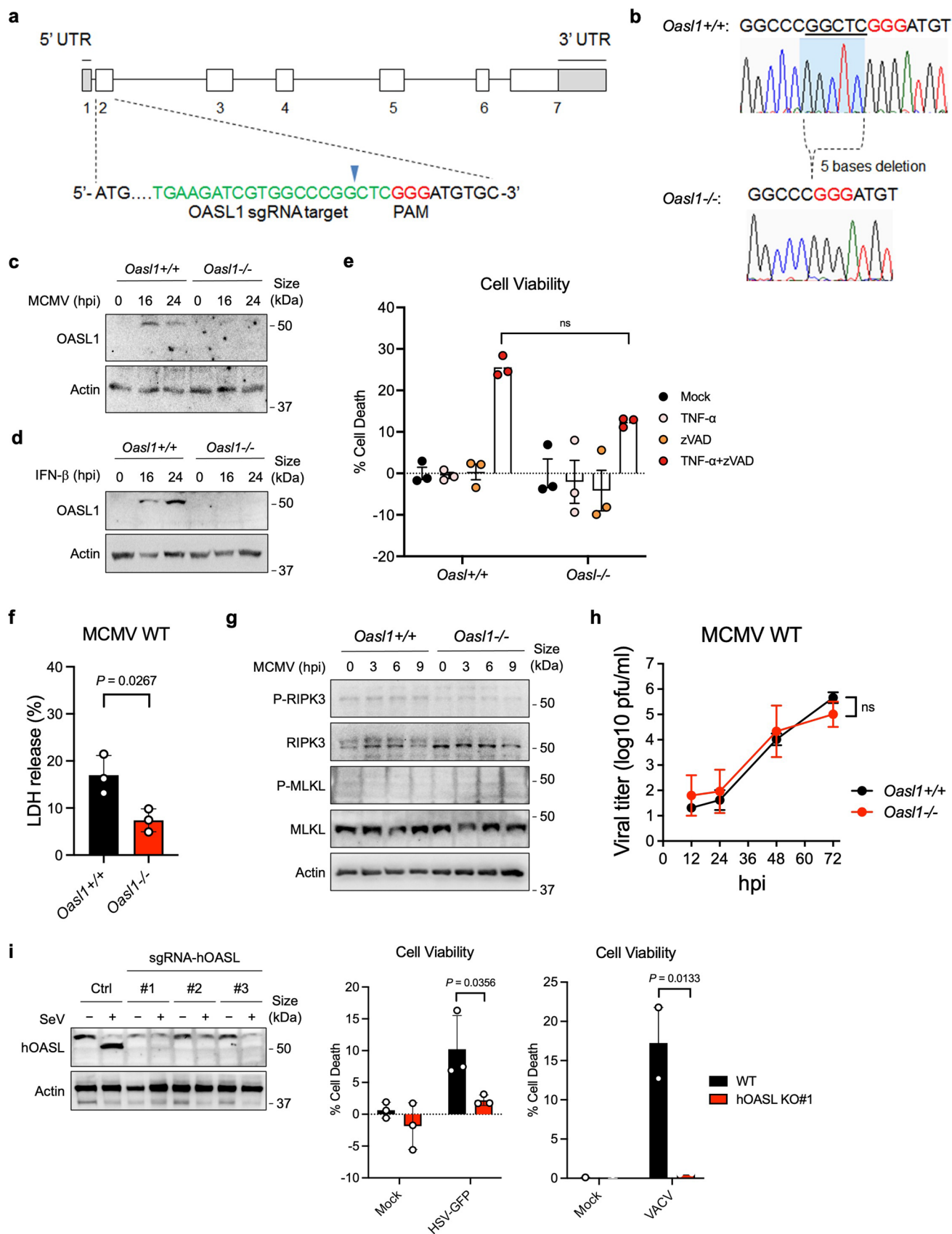
Extended data is available for this paper at <https://doi.org/10.1038/s41556-022-01039-y>.

Supplementary information The online version contains supplementary material available at <https://doi.org/10.1038/s41556-022-01039-y>.

Correspondence and requests for materials should be addressed to Shin-Ae Lee, Lin-Chun Chang or Jae U. Jung.

Peer review information *Nature Cell Biology* thanks Zhengfan Jiang and Andrew Oberst for their contribution to the peer review of this work.

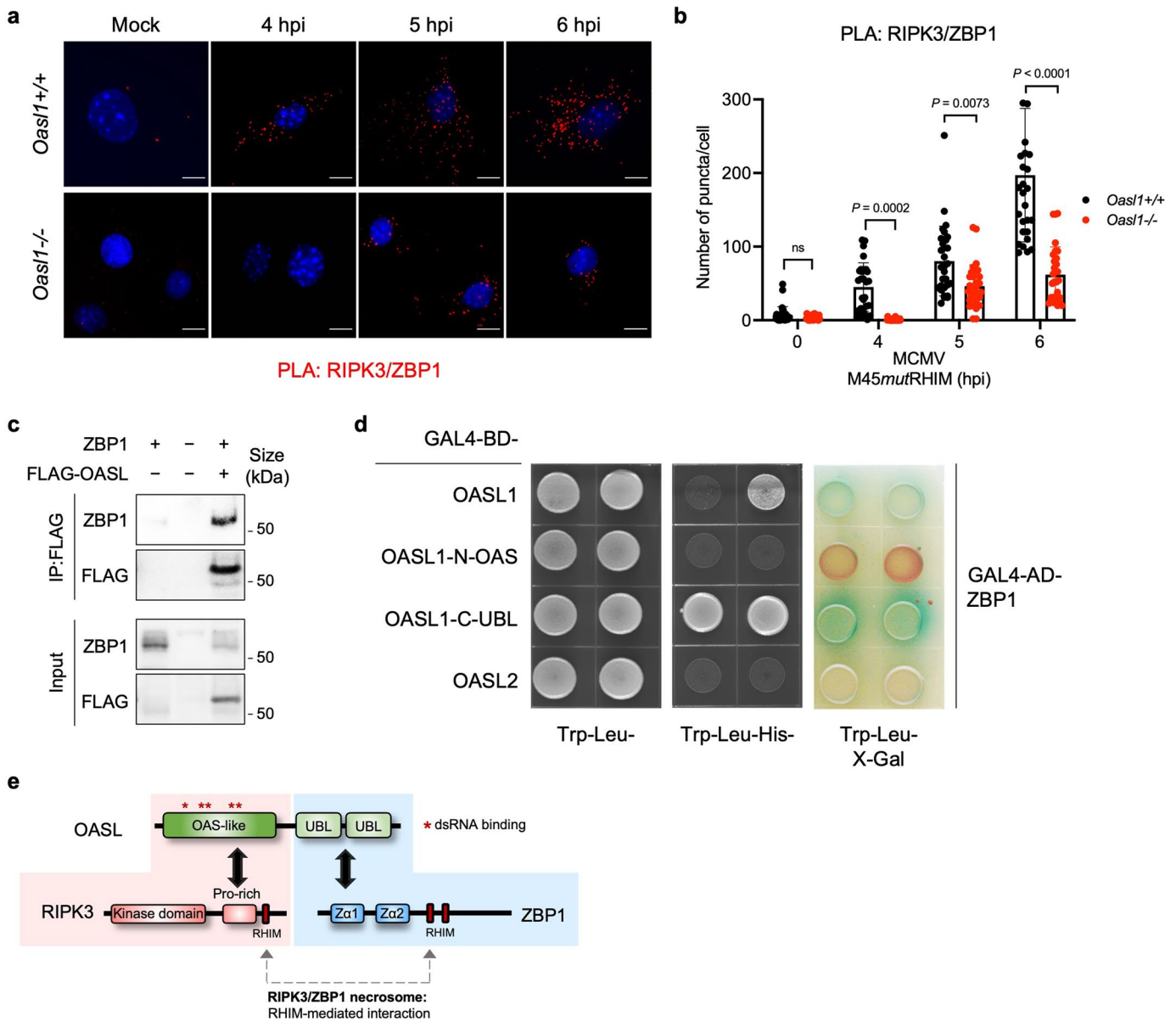
Reprints and permissions information is available at www.nature.com/reprints.



Extended Data Fig. 1 | See next page for caption.

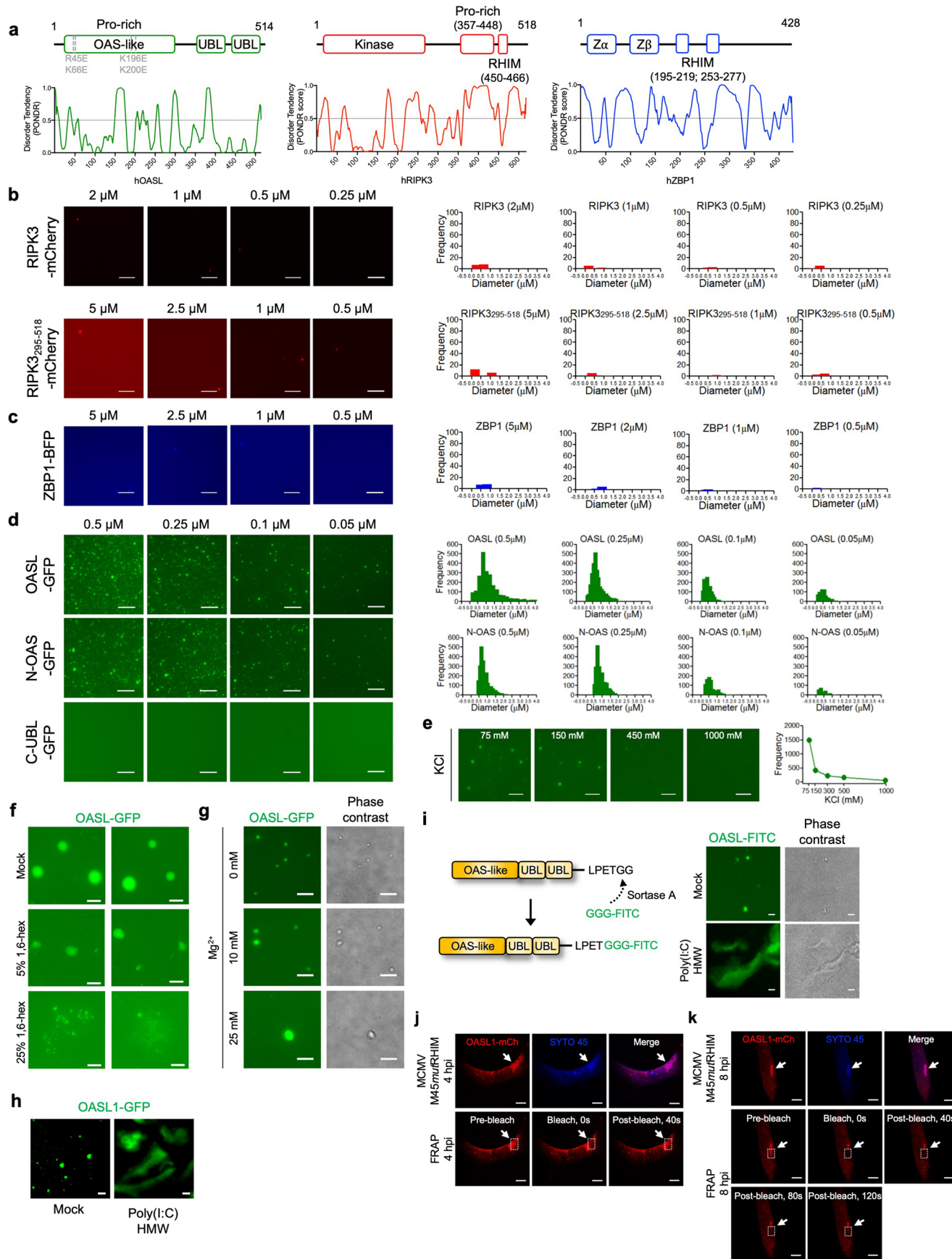
Extended Data Fig. 1 | Generation of *Oasl1*^{-/-} mouse using the CRISPR-Cas9 system and the function of *Oasl1* in virus-induced necroptosis. a, Schematic of the genomic target in *OASL1* gene and *OASL1* exon 2 sgRNA. The sgRNA sequence (designed in <http://chopchop.cbu.uib.no>) is marked in green and the protospacer adjacent motif (PAM) sequence is marked in red. Blue arrow points the predicted cleavage site. **b**, Mouse *Oasl1* genomic sequences from *Oasl1*^{+/+} and *Oasl1*^{-/-} littermate mice. PAM sequence is marked in red. 5 base pairs deletion was shown in *Oasl1*^{-/-} mice. **c,d**, Immunoblot analysis of OASL1 expression in *Oasl1*^{+/+} and *Oasl1*^{-/-} primary fibroblasts infected with MCMV (**c**) or treated with IFN- β (**d**) for the indicated times. **e**, Quantification of necrotic cell death by measuring the intracellular ATP levels in *Oasl1*^{+/+} and *Oasl1*^{-/-} primary fibroblasts upon TNF- α (50 ng/ml) and/or zVAD (20 mM) treatment. **f**, Measurement of lactate dehydrogenase (LDH) release to the medium in *Oasl1*^{+/+} or *Oasl1*^{-/-} primary fibroblasts infected with MCMV-WT (m.o.i. = 5) for 8 h. **g**, Immunoblot analysis

of RIPK3 and MLKL phosphorylation in *Oasl1*^{+/+} or *Oasl1*^{-/-} primary fibroblasts infected with MCMV-WT (m.o.i. = 5) for the indicated hours. **h**, MCMV-WT titer in *Oasl1*^{+/+} and *Oasl1*^{-/-} primary fibroblasts were determined by plaque assays by titrating culture medium at the indicating time points ($n = 4$ for *Oasl1*^{+/+}, $n = 2$ for *Oasl1*^{-/-}). **i**, (Left) Immunoblot analysis of CRISPR Cas9-mediated knockout of human OASL in A549 cells upon mock or Sendai virus (SeV) infection (Asterisk, non-specific band). Quantification of necrotic cell death by measuring the intracellular ATP levels in WT and hOASL KO A549 cells infected with (middle) HSV-GFP (m.o.i. = 10) upon IFN- β stimulation ($n = 3$) or (right) VACV (m.o.i. = 5) ($n = 2$). **c,d,g**, Data are representative of two independent experiments. **e,f**, Data are presented as mean \pm SEM from three independent experiments. Statistical analyses were performed using a two-tailed unpaired *t*-test (**f**) or two-way analysis of variance (ANOVA) (**e,h,i**). ns, not significant.



Extended Data Fig. 2 | OASL interacts with RIPK3 and ZBP1 through its N-OAS and C-UBL domain, respectively. a, *In situ* proximity ligation assay (PLA) of RIPK3 and ZBP1 in *Oas1*^{+/+} and *Oas1*^{-/-} primary fibroblasts infected with mock or MCMV-M45mutRHIM (m.o.i. = 5) for the indicated hours. Fluorescence microscope was used to detect the discrete fluorescent PLA signals (red dots). Representative images of dots indicate the interaction of endogenous RIPK3 and ZBP1. **b**, Quantification of dot signals of **a** per cell (*n* = 30 cells). Each dot indicates single cell. **c**, HEK 293 T cells were transfected with the indicated FLAG or untagged constructs, and cell lysates were immunoprecipitated with

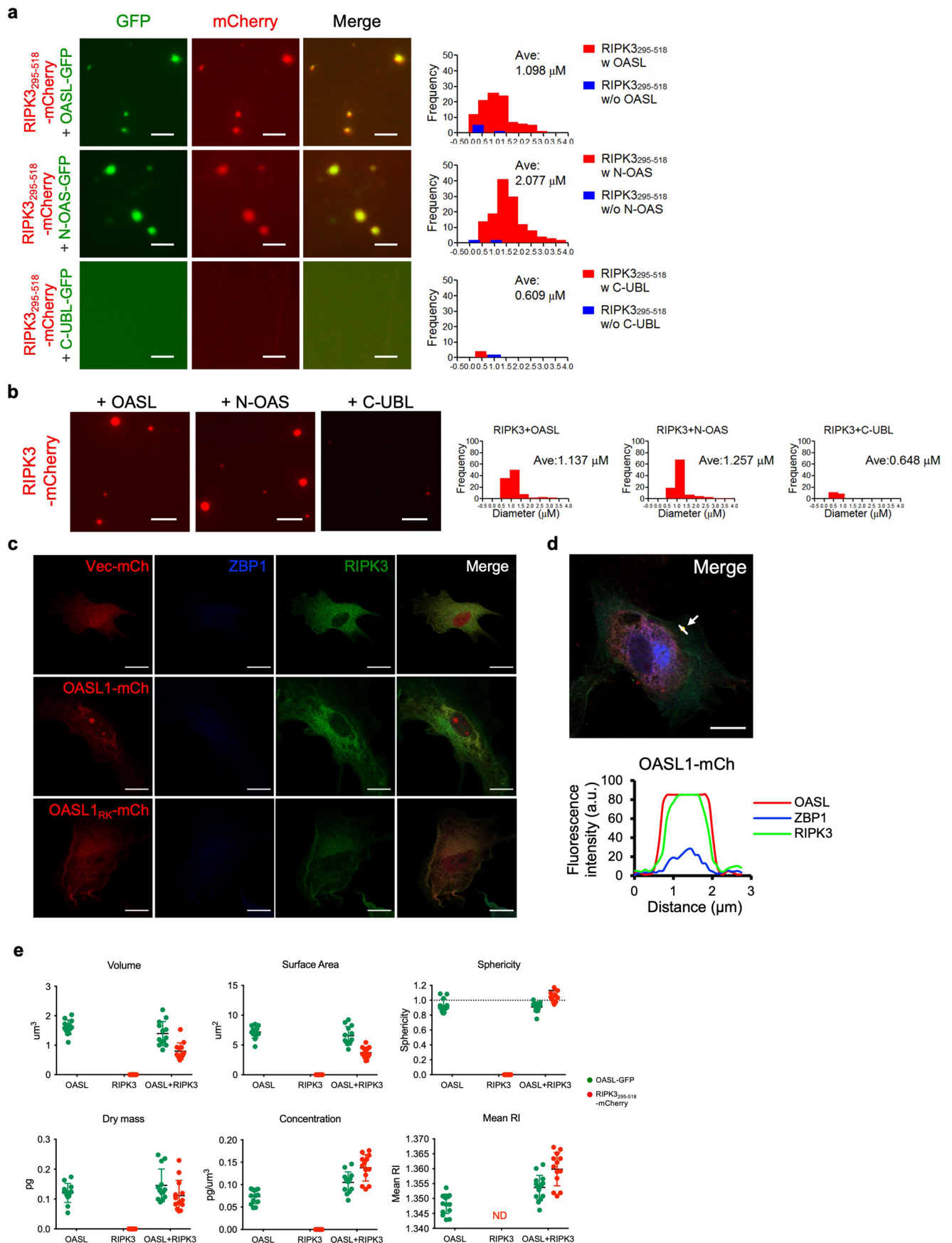
anti-FLAG antibody. Immunoprecipitates and whole cell extracts (input) were analyzed by immunoblotting with the indicated antibodies. **d**, AH109 yeasts were transformed with the indicated pGBKT7 or pACT2 constructs. Interactions were measured by triple dropout (Trp-Leu-His-) synthetic medium or secreted α -galactosidase activity assays using X- α Gal. **e**, Schematic of the interaction of OASL with RIPK3 and ZBP1 through its N-terminus and C-terminus domains, respectively. **a-d**, Data are representative of two independent experiments with similar results. **b**, Data are presented as mean \pm SEM and statistical analysis was performed using two-way ANOVA.



Extended Data Fig. 3 | See next page for caption.

Extended Data Fig. 3 | Liquid-liquid phase separation properties of OASL, RIPK3, and ZBP1. **a**, Graph of putative intrinsically disordered regions of human OASL, RIPK3, and ZBP1 as calculated by PONDR (VSL2) algorithm. **b**, Failure of liquid droplet formation of purified mCherry-tagged full-length RIPK3 or C-terminal RIPK3₂₉₅₋₅₁₈. Scale bar, 10 μm . **c**, Failure of liquid droplet formation of purified BFP-tagged full-length ZBP1. Scale bar, 10 μm . **d**, *In vitro* droplet formation by GFP-tagged full-length OASL, N-OAS, or C-UBL protein in a concentration-dependent manner. Incubation was carried out at physiological temperature and buffer for 1 h. Scale bar, 10 μm . **b-d**, Histogram represent distribution of quantified droplet amounts and diameters of the liquid droplets. **e**, Effect of KCl concentration on the formation of OASL liquid droplets. Scale bar, 10 μm . **f**, OASL-GFP droplets treated with increasing concentration of

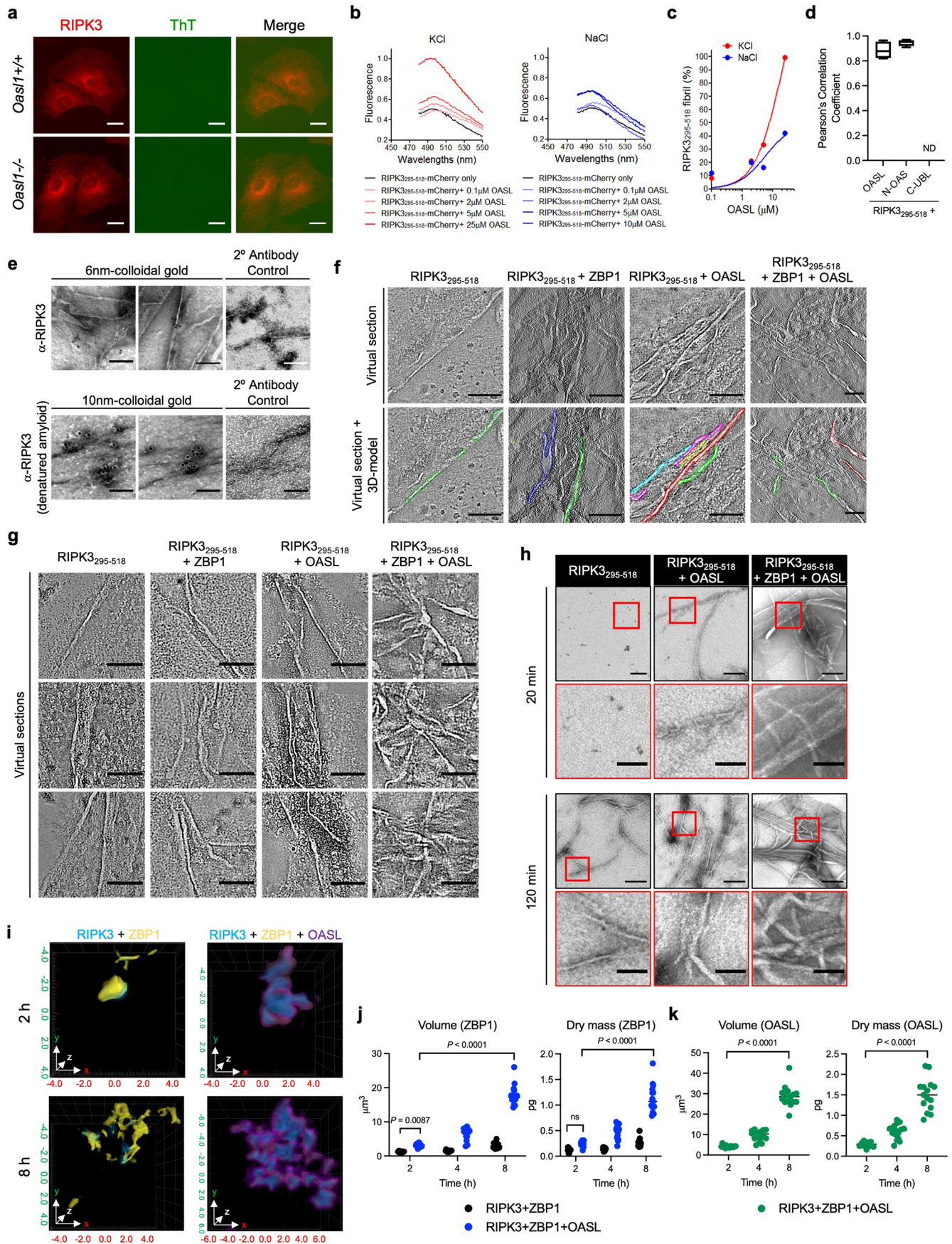
1,6-hexanediol. Scale bar, 5 μm . **g**, Increase of Mg^{2+} concentration leads to enlargement of OASL droplets. Scale bar, 10 μm . **h**, *In vitro* liquid droplet formation of GFP-tagged mouse OASL (OASL1) treated with mock or poly(I:C) HMW (50 $\mu\text{g}/\text{ml}$) for 1 h. Scale bar, 10 μm . **i**, (Left) Schematic diagram of Sortase A-mediated labeling of FITC at the C-terminus of OASL with Sortase A-recognition motif (LPETGG). (Right) *In vitro* phase separation of FITC-labeled OASL treated with mock or poly(I:C) HMW (50 $\mu\text{g}/\text{ml}$). Scale bar, 10 μm . **j,k**, Representative FRAP images of OASL1 foci observed at (j) 4 h.p.i. and (k) 8 h.p.i. (l), SYTO 45-stained OASL1-Cherry foci were chosen for photobleaching. White rectangle box indicates the photobleached and recovered area within the foci. Scale bar, 10 μm . Data are representative of three (b-i) or two (j,k) independent experiments with similar results.



Extended Data Fig. 4 | See next page for caption.

Extended Data Fig. 4 | OASL liquid phase separation during virus-induced necroptosis. **a**, (Left) Representative images of liquid droplet formation of GFP-tagged full-length OASL, N-terminus OAS-like domain, or C-terminus UBL domain with mCherry-tagged RIPK3₂₉₅₋₅₁₈. Scale bar, 5 μ m. (Right) Histogram of the size and formation frequency of RIPK3₂₉₅₋₅₁₈-mCherry droplets with or without the presence of GFP-tagged OASL proteins. **b**, (Left) Full length RIPK3-mCherry undergoes phase separation in the presence of purified OASL or N-OAS, but not C-UBL. Representative images of liquid droplet formation of mCherry-tagged full-length RIPK3 in the presence of full-length OASL, N-OAS or C-UBL. 2 μ M of RIPK3-mCherry was mixed with 0.5 μ M of purified OASL proteins. Scale bar, 5 μ m. (Right) Histogram of the size and formation frequency of RIPK3 droplets. **c**, Confocal imaging of mock-infected *Oas1l*^{-/-} primary fibroblasts reconstituted

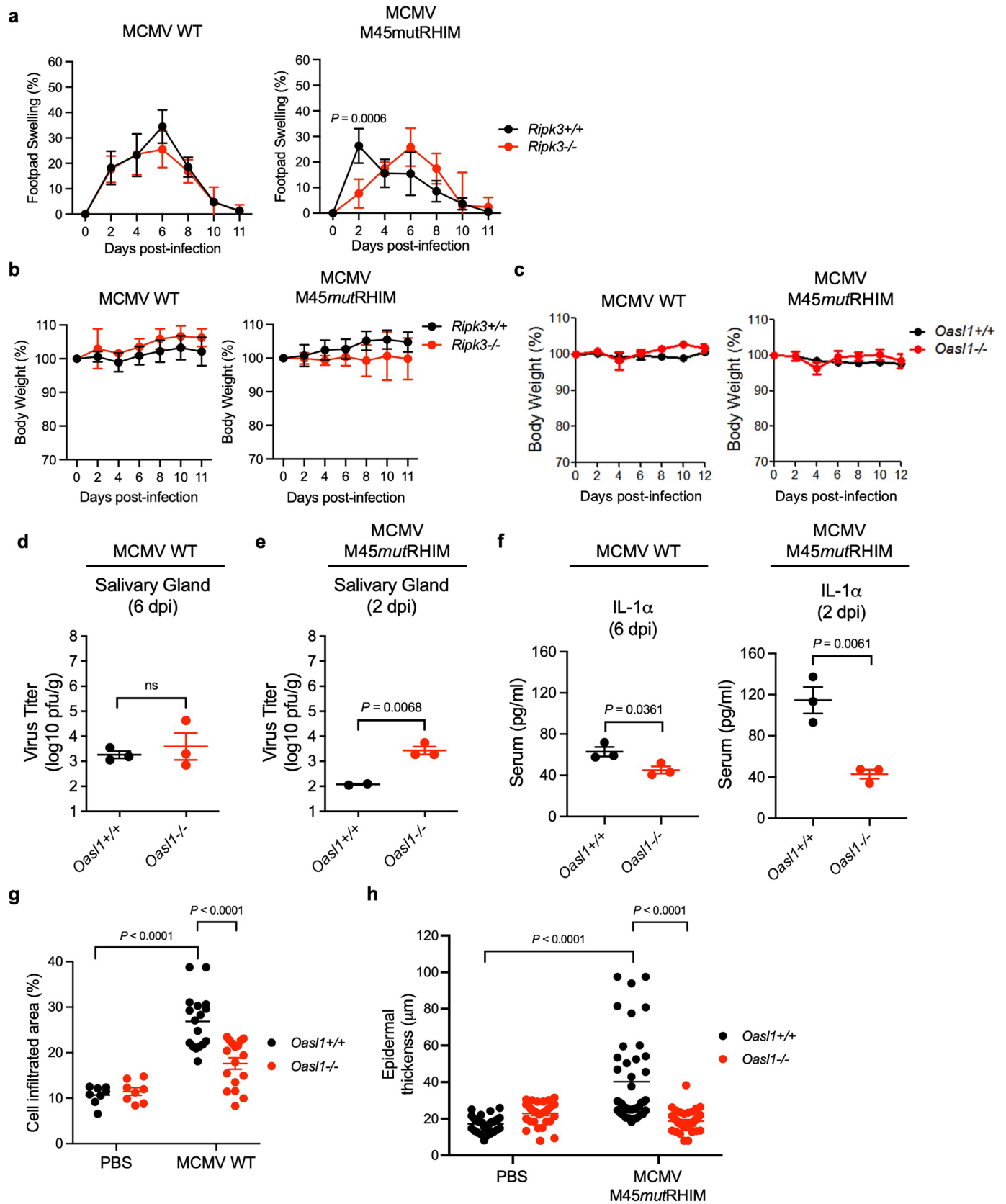
with mCherry-tagged vector, OASL1, or OASL1_{RRK}. Scale bar, 10 μ m. **d**, (Top) OASL1-mCherry merged image of Fig. 4c with line across the condensate. Scale bar, 10 μ m. (Bottom) Line profile of fluorescence intensity indicates colocalization of OASL1, ZBP1, and RIPK3 signal in OASL1-mCherry expressing *Oas1l*^{-/-} primary fibroblasts. **e**, Quantitative analysis of morphological (top) and biochemical (bottom) parameters of OASL-GFP alone, RIPK3₂₉₅₋₅₁₈-mCherry alone, and OASL-GFP with RIPK3₂₉₅₋₅₁₈-Cherry liquid-like droplets before and after incubation at physiological conditions ($n = 13$ condensates per group). Morphological parameters include volumes, surface areas, and sphericity. Biochemical parameters include dry mass, concentration, and mean RI. ND, not detected. Data are representative of three (**a-c**) or two (**e**) independent experiments with similar results.



Extended Data Fig. 5 | See next page for caption.

Extended Data Fig. 5 | OASL phase separation promotes RIPK3 amyloid fibrillation. **a**, Representative images of mock-infected *Oasl1^{+/+}* and *Oasl1^{-/-}* primary fibroblasts immunostained for endogenous RIPK3 and amyloid-like structure by anti-RIPK3 antibody and Thioflavin T (ThT), respectively. Scale bar, 10 μm . **b**, Fibrillation of RIPK3₂₉₅₋₅₁₈-mCherry in vitro with increasing amounts of OASL at physiological (left) KCl or (right) NaCl concentration for 16 h. **c**, Dose-response curve of OASL inducing RIPK3₂₉₅₋₅₁₈-mCherry fibrillation assessed by ThT emission. **d**, Quantification of RIPK3₂₉₅₋₅₁₈-mCherry and ThT signal colocalization upon incubation with OASL, N-OAS, or C-UBL. Box plots show the minimum, first quartile, median, third quartile, and maximum with $n = 150$ droplets per group. **e**, TEM imaging of RIPK3₂₉₅₋₅₁₈-mCherry fibrils after phase separation with ZBP1-BFP and OASL-GFP, followed by immunogold-labeling with anti-RIPK3 antibody upon (top) normal or (bottom) denatured condition. Prominent immunogold labeling was observed in denatured

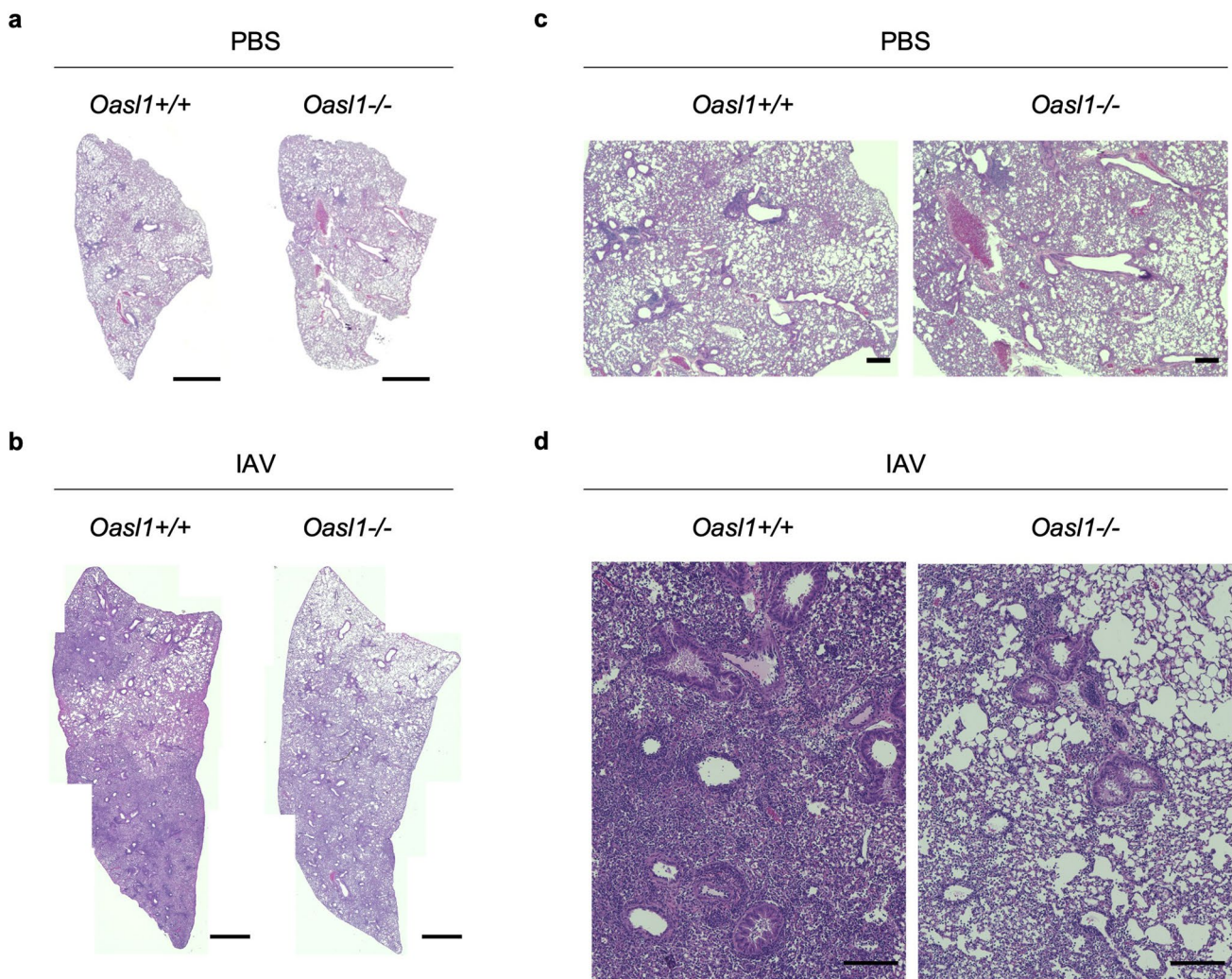
condition. **f**, Virtual sections of RIPK3 amyloid fibrils through the tomogram and overlays with 3D-model at different z-axis positions. **g**, Virtual sections of RIPK3₂₉₅₋₅₁₈-mCherry fibrils through tomogram at different z-axis positions. **h**, TEM images of RIPK3₂₉₅₋₅₁₈-mCherry alone or incubated with OASL or OASL and ZBP1 together after 20 or 120 min of phase separation. Scale bar, 200 nm. Insets: magnified views of the red box regions. **e-h**, Scale bar, 100 nm. **i**, Representative 3D refractive index distribution of RIPK3 + ZBP1 or RIPK3 + ZBP1 + OASL at the indicated times. RI tomogram: blue (RIPK3), yellow (ZBP1), purple (OASL). ($n = 30$ condensates per condition). **j,k**, 3D tomogram quantitative analysis of ZBP1-BFP (**j**) and OASL-GFP (**k**) upon co-incubation with RIPK3 ($n = 15$ condensates per group). Data are representative of three (**a-d**) or two (**i-k**) independent experiments with similar results. **e-h**, TEM images are representative of at least 8 fields with four independent experiments. **j,k**, Data are presented as mean \pm SEM and statistical analyses were performed using two-way ANOVA. ND, not detected.



Extended Data Fig. 6 | See next page for caption.

Extended Data Fig. 6 | Murine OASL1 is required for MCMV infection-induced necroptosis to restrict viral dissemination *in vivo*. **a**, Measurement of footpad swelling caused by subcutaneous footpad injection of *Ripk3*^{+/+} or *Ripk3*^{-/-} mice with 10⁶ PFU (left) MCMV-WT (*n* = 4 per genotype) or (right) MCMV-M45mutRHIM (*Ripk3*^{+/+}; *n* = 5, except *n* = 3 for 6 d.p.i.; *Ripk3*^{-/-}; *n* = 5 for 0-4, 10 d.p.i., *n* = 3 for 6, 8, 11 d.p.i.). Data are represented as the percent increase in thickness relative to the pre-injection measurement and plotted for mean values at the indicated times. **b, c**, Body weight changes of **a** *Ripk3*^{+/+} and *Ripk3*^{-/-} mice infected with MCMV-WT (*n* = 4 per genotype) and MCMV-M45mutRHIM infection (*n* = 5 per genotype) and **Fig. 6a, b** *Oasl1*^{+/+} and *Oasl1*^{-/-} littermate mice infected with MCMV-WT (*n* = 8 for *Oasl1*^{+/+} and *n* = 6 for *Oasl1*^{-/-}) or MCMV-M45mutRHIM (*n* = 8 mice per genotype). **d, e**, Viral titers in salivary glands (SG) from *Oasl1*^{+/+} and *Oasl1*^{-/-} littermate mice infected with **(d)** MCMV-WT (*n* = 3 mice

per genotype) or **(e)** MCMV-M45mutRHIM (*n* = 2 for *Oasl1*^{+/+} and *n* = 3 for *Oasl1*^{-/-}) at the indicated days post-footpad subcutaneous injection. **f**, IL-1 α levels in the sera of *Oasl1*^{+/+} and *Oasl1*^{-/-} mice infected with MCMV-WT or MCMV-M45mutRHIM at the indicated days were determined by ELISA (*n* = 3 mice per genotype). **d-f**, Each symbol represents one mouse, horizontal lines represent the mean value. **g, h**, Quantification of Fig. 6e cell infiltration (*n* = 8 per genotype for PBS, *n* = 17 per genotype for MCMV-WT) and footpad epidermal thickness (*n* = 31 per genotype for PBS, *n* = 41 per genotype for MCMV-M45mutRHIM) in mice infected with MCMV-WT or MCMV-M45mutRHIM at 2 or 6 d.p.i., respectively. All data are pooled from three independent experiments. **d-h** Data are presented as mean \pm SEM. Statistical analyses were performed using a two-tailed unpaired *t*-test (**d-f**) or two-way ANOVA (**a, g, h**).



Extended Data Fig. 7 | OASL1 is required for influenza virus infection-induced immune cell infiltration. a,b, H&E staining of whole lung sections of *Oasl1*^{+/+} and *Oasl1*^{-/-} littermate mice intranasally-inoculated with (a) PBS or (b) 100 PFU of IAV PR8 at 7 d.p.i. Scale bar, 1 mm. **c,d**, Representative histology of lung sections of **a,b**, respectively. Scale bar, 200 μm.

Reporting Summary

Nature Portfolio wishes to improve the reproducibility of the work that we publish. This form provides structure for consistency and transparency in reporting. For further information on Nature Portfolio policies, see our [Editorial Policies](#) and the [Editorial Policy Checklist](#).

Statistics

For all statistical analyses, confirm that the following items are present in the figure legend, table legend, main text, or Methods section.

n/a Confirmed

- The exact sample size (n) for each experimental group/condition, given as a discrete number and unit of measurement
- A statement on whether measurements were taken from distinct samples or whether the same sample was measured repeatedly
- The statistical test(s) used AND whether they are one- or two-sided
Only common tests should be described solely by name; describe more complex techniques in the Methods section.
- A description of all covariates tested
- A description of any assumptions or corrections, such as tests of normality and adjustment for multiple comparisons
- A full description of the statistical parameters including central tendency (e.g. means) or other basic estimates (e.g. regression coefficient) AND variation (e.g. standard deviation) or associated estimates of uncertainty (e.g. confidence intervals)
- For null hypothesis testing, the test statistic (e.g. F , t , r) with confidence intervals, effect sizes, degrees of freedom and P value noted
Give P values as exact values whenever suitable.
- For Bayesian analysis, information on the choice of priors and Markov chain Monte Carlo settings
- For hierarchical and complex designs, identification of the appropriate level for tests and full reporting of outcomes
- Estimates of effect sizes (e.g. Cohen's d , Pearson's r), indicating how they were calculated

Our web collection on [statistics for biologists](#) contains articles on many of the points above.

Software and code

Policy information about [availability of computer code](#)

Data collection

1. Immunofluorescence images were acquired using NIS-Elements Confocal (Nikon), BZ-X710 microscope software (Keyence), and LAS X (Leica).
2. FRAP assay was performed using Zen (Zeiss).
3. 3D holotomography imaging was performed using TomoStudio (Tomocube).
4. TEM imaging was performed using EM-MENU software (TVIPS) or Tecnai Spirit G2, FEI software.
5. Immunoblotting data were imaged using Chemidoc Chemiluminescence system (Bio-Rad).
6. qRT-PCR data were acquired using CFX Manager 3.1 software (Bio-Rad).

Data analysis

Statistical analysis was performed using Prism v9.1 (GraphPad). FRAP analysis was performed using Zen black edition v3.0 (Zeiss). Holotomography image analysis was performed using TomoStudio v2.6.15 (Tomocube). TEM image analysis was performed using IMOD (v4.11.2). All other image analyses were performed using Image J (FIJI).

For manuscripts utilizing custom algorithms or software that are central to the research but not yet described in published literature, software must be made available to editors and reviewers. We strongly encourage code deposition in a community repository (e.g. GitHub). See the Nature Portfolio [guidelines for submitting code & software](#) for further information.

Data

Policy information about [availability of data](#)

All manuscripts must include a [data availability statement](#). This statement should provide the following information, where applicable:

- Accession codes, unique identifiers, or web links for publicly available datasets
- A description of any restrictions on data availability
- For clinical datasets or third party data, please ensure that the statement adheres to our [policy](#)

Data that support the findings of this study are available from the corresponding author upon request.

Field-specific reporting

Please select the one below that is the best fit for your research. If you are not sure, read the appropriate sections before making your selection.

- Life sciences Behavioural & social sciences Ecological, evolutionary & environmental sciences

For a reference copy of the document with all sections, see [nature.com/documents/nr-reporting-summary-flat.pdf](https://www.nature.com/documents/nr-reporting-summary-flat.pdf)

Life sciences study design

All studies must disclose on these points even when the disclosure is negative.

Sample size	No statistical methods were used to predetermine sample size. Sample size was determined based on the numbers required to generate statistical power and preliminary experiments.
Data exclusions	No data were excluded from the analyses.
Replication	All experiments were independently repeated at least twice to ensure reproducibility of findings. Details are clearly indicated in each figure legend.
Randomization	All animals were assigned to groups randomly.
Blinding	Blinding was not relevant to the study.

Reporting for specific materials, systems and methods

We require information from authors about some types of materials, experimental systems and methods used in many studies. Here, indicate whether each material, system or method listed is relevant to your study. If you are not sure if a list item applies to your research, read the appropriate section before selecting a response.

Materials & experimental systems

n/a	Involved in the study
<input type="checkbox"/>	<input checked="" type="checkbox"/> Antibodies
<input type="checkbox"/>	<input checked="" type="checkbox"/> Eukaryotic cell lines
<input checked="" type="checkbox"/>	<input type="checkbox"/> Palaeontology and archaeology
<input type="checkbox"/>	<input checked="" type="checkbox"/> Animals and other organisms
<input checked="" type="checkbox"/>	<input type="checkbox"/> Human research participants
<input checked="" type="checkbox"/>	<input type="checkbox"/> Clinical data
<input checked="" type="checkbox"/>	<input type="checkbox"/> Dual use research of concern

Methods

n/a	Involved in the study
<input checked="" type="checkbox"/>	<input type="checkbox"/> ChIP-seq
<input checked="" type="checkbox"/>	<input type="checkbox"/> Flow cytometry
<input checked="" type="checkbox"/>	<input type="checkbox"/> MRI-based neuroimaging

Antibodies

Antibodies used

Human RIPK3 (Cell Signaling Technology; Cat# 13526; E1Z1D; Lot# 3)
 Human p-RIPK3 (Cell Signaling Technology; Cat# 93654; D6W2T; Lot# 2)
 Mouse RIPK3 (Cell Signaling Technology; Cat# 95702; D4G2A; Lot# 3)
 Mouse p-RIPK3 (Cell Signaling Technology; Cat# 57220; E7S1R; Lot# 1)
 Mouse MLKL (Cell Signaling Technology; Cat# 37705; D6W1K; Lot# 1)
 Mouse p-MLKL (Cell Signaling Technology; Cat# 37333; D6E3G; Lot# 2)
 Human OASL (Santa Cruz; Cat# sc-130832; L-25; Lot# A2214)
 Mouse OASL1 (Gifted by Dr. Myeong Sup Lee)
 ZBP1 (AdipoGen; Cat# AG-20B-0010-C100; Zippy-1; Lot#A28231605)
 PKR (Santa Cruz; Cat# sc-707; K-17; Lot# F1214)
 Actin (Santa Cruz; Cat# sc-47778; C4; Lot# J1512)

Mouse-HA (BioLegend; Cat# 901503; 16B12; Lot# B200768)
 Rabbit-HA (BioLegend; Cat# 902301; PRB-101P; Lot# E11BF00)
 Mouse-FLAG (Sigma; Cat# F1804; Lot# SLBR7936V)
 Rabbit-FLAG (Sigma; Cat# F7425; Lot# 086M4803V)
 Mouse-V5 (Thermo Fisher; Cat# R960-25; Lot# 2184509)
 Rabbit Alexa Fluor 488 (Thermo Fisher; Cat# A11008; Lot# 2018309)
 Rabbit Alexa Fluor 568 (Thermo Fisher; Cat# A11011; Lot# 2192277)
 Mouse Alexa Fluor 568 (Thermo Fisher; Cat# A10037; Lot# 2110843)
 Mouse Cascade Blue (Thermo Fisher; Cat# C962; Lot# 1316675)

Validation

Each primary antibody was validated for the species and application according to previous publications and the manufacturers' datasheet, which are available on the manufacturer website. The antibodies were further validated internally and routinely used in the lab. Data are provided and details are reported in Methods.

Eukaryotic cell lines

Policy information about [cell lines](#)

Cell line source(s)

HEK-293T, NIH3T3, Vero, and A549 cells were obtained from ATCC.
 Primary murine fibroblasts were obtained from C57BL/6 mice.

Authentication

Cell lines were not authenticated.

Mycoplasma contamination

All cell lines were tested negative for mycoplasma contamination.

Commonly misidentified lines
(See [ICLAC](#) register)

No commonly misidentified cell lines were used.

Animals and other organisms

Policy information about [studies involving animals](#); [ARRIVE guidelines](#) recommended for reporting animal research

Laboratory animals

Wild-type, Oasl1^{-/-}, and Ripk3^{-/-} mice are C57BL/6 genetic background. 3-4-week-old mice of equal distribution were used for primary fibroblast isolation from the tail. 6-8-week-old age mice of equal distribution were used for in vivo experiments. Details are reported in Methods.

Wild animals

Study did not involve wild animals.

Field-collected samples

Study did not involve samples collected from the field.

Ethics oversight

All mice were used in accordance with protocols and ethical regulations approved by the University of Southern California and Cleveland Clinic Institutional Animal Care and Use Committee.

Note that full information on the approval of the study protocol must also be provided in the manuscript.